Structure–function mapping of a heptameric module in the nuclear pore complex

Javier Fernandez-Martinez,[1] Jeremy Phillips,[3,4,5] Matthew D. Sekedat,[2] Ruben Diaz-Avalos,[6] Javier Velazquez-Muriel,[3,4,5] Josef D. Franke,[1] Rosemary Williams,[1] David L. Stokes,[6] Brian T. Chait,[2] Andrej Sali,[3,4,5] and Michael P. Rout[1]

[1]Laboratory of Cellular and Structural Biology and [2]Laboratory of Mass Spectrometry and Gaseous Ion Chemistry, The Rockefeller University, New York, NY 10065
[3]Department of Bioengineering and Therapeutic Sciences, [4]Department of Pharmaceutical Chemistry, and [5]California Institute for Quantitative Biosciences, University of California, San Francisco, San Francisco, CA 94158
[6]The New York Structural Biology Center, New York, NY 10027

The nuclear pore complex (NPC) is a multiprotein assembly that serves as the sole mediator of nucleocytoplasmic exchange in eukaryotic cells. In this paper, we use an integrative approach to determine the structure of an essential component of the yeast NPC, the ∼600-kD heptameric Nup84 complex, to a precision of ∼1.5 nm. The configuration of the subunit structures was determined by satisfaction of spatial restraints derived from a diverse set of negative-stain electron microscopy and protein domain–mapping data. Phenotypic data were mapped onto the complex, allowing us to identify regions that stabilize the NPC's interaction with the nuclear envelope membrane and connect the complex to the rest of the NPC. Our data allow us to suggest how the Nup84 complex is assembled into the NPC and propose a scenario for the evolution of the Nup84 complex through a series of gene duplication and loss events. This work demonstrates that integrative approaches based on low-resolution data of sufficient quality can generate functionally informative structures at intermediate resolution.

Introduction

Cells are comprised of thousands of highly organized, complex, and dynamic subcellular macromolecular assemblies. To study how cells function, we need methodologies to determine the structures, dynamics, and interactions of these assemblies and thus reveal how they give rise to the emergent properties of life. One such dynamic macromolecular assembly is the nuclear pore complex (NPC), the gatekeeper within the nuclear envelope (NE) that mediates the exchange of specific macromolecules between the nucleoplasm and cytoplasm. Every NPC is formed by ∼30 different proteins called nucleoporins (nups), each present in multiple copies and connected in biochemically stable subcomplexes that act as building blocks for the NPC (D'Angelo and Hetzer, 2008; Strambio-De-Castillia et al., 2010).

The NPC structural core is conserved, highly modular, and is formed from eight symmetric spokes that connect to form five coaxial rings: a membrane ring, two adjacent inner rings, and two outer rings facing, respectively, the cytoplasmic and nucleoplasmic periphery (Alber et al., 2007b). Proteins termed FG (phenylalanine–glycine) nups fill the central channel of the NPC and establish the permeability barrier (Peters, 2009; Strambio-De-Castillia et al., 2010). Analysis of the fold composition of the NPC led to our proposal of the protocoatomer hypothesis (Devos et al., 2004, 2006), which suggests a common ancestry for the NPC and membrane-coating complexes; they are thought to have evolved by divergent evolution from a protocoatomer membrane–bending complex present in the last eukaryotic common ancestor (DeGrasse et al., 2009; Field et al., 2011).

Data from both vertebrates and the yeast *Saccharomyces cerevisiae* (Rout et al., 2000; Belgareh et al., 2001; Krull et al., 2004; Alber et al., 2007b) indicate that the outer ring of the NPC

Supplemental Material can be found at:
http://jcb.rupress.org/content/suppl/2012/02/09/jcb.201109008.DC1.html

The Rockefeller University Press $30.00
J. Cell Biol. Vol. 196 No. 4 419–434
www.jcb.org/cgi/doi/10.1083/jcb.201109008

JCB 419

is comprised of a conserved assembly, which in vertebrates corresponds to a nonameric complex called the Nup107–160 complex (Belgareh et al., 2001; Vasu et al., 2001; Loïodice et al., 2004) and in yeast corresponds to the Nup84 complex, which is formed from seven proteins named Nup133, Nup120, Nup145c, Nup85, Nup84, Seh1, and Sec13 (Siniossoglou et al., 1996; Lutzmann et al., 2002). Sec13 is shared with the Sec13/31 COPII vesicle-coating complex (VCC), and both Seh1 and Sec13 have recently been found in a coating-related complex termed the Seh1-associated complex, underscoring the relationship between coatomers and NPCs (Siniossoglou et al., 1996; Salama et al., 1997; Devos et al., 2004; Dokudovskaya et al., 2011).

The Nup84 complex is the best characterized of the NPC's building blocks, as reflected by the extensive set of genetic, biochemical, and structural data accumulated over the years (Doye and Hurt, 1995; Fabre and Hurt, 1997; Brohawn et al., 2009). Mutations of Nup84 complex nups usually lead to severe phenotypes characterized by fitness defects, mRNA, and preribosomal export problems as well as aberrant NPC biogenesis and distribution (i.e., clustering of NPCs into a handful of closely packed groups) within the NE; indeed, the NPC clustering phenotype has been broadly used as a tool to characterize putative NPC-associated proteins (Doye et al., 1994; Aitchison et al., 1995; Heath et al., 1995; Li et al., 1995; Pemberton et al., 1995). The Nup84 heptamer forms a characteristic Y-shaped assembly, as shown by pioneering EM studies of both isolated complexes and complexes reconstituted in vitro; Nup133, Nup84, and Nup145c/Sec13 form the main stalk of the Y, with Nup133 at its tip, and Nup85/Seh1 and Nup120 are located in the two short arms of the heptameric assembly (Siniossoglou et al., 2000; Lutzmann et al., 2002; Kampmann and Blobel, 2009).

Structural analyses by combined computational and biochemical methods (Devos et al., 2004, 2006) and subsequent crystallographic studies (Hsia et al., 2007; Boehmer et al., 2008; Brohawn et al., 2008; Debler et al., 2008; Brohawn and Schwartz, 2009; Leksa et al., 2009; Nagy et al., 2009; Seo et al., 2009; Whittle and Schwartz, 2009; Sampathkumar et al., 2011) have shown that nups within the Nup84 complex are formed almost entirely by a β-propeller fold, an α-solenoid–like fold (or helix-turn-helix repeat, which from now on we will refer to as α-solenoid), or a combination of N-terminal β-propeller and C-terminal α-solenoid–like folds (termed a β-α fold arrangement), again common to VCCs. Despite this wealth of data, we still do not have a full description of the structures or domain interfaces in the Nup84 complex (Brohawn et al., 2009); moreover, differing interpretations of the crystallographic structures have led to models of the arrangement of the Nup84 complex in the NPC (Debler et al., 2008; Brohawn et al., 2009) that do not agree with each other nor with maps from other groups in the field (Belgareh et al., 2001; Krull et al., 2004), including our own (Alber et al., 2007b). Such ambiguities are frequently observed in the structure determination of protein assemblies (Robinson et al., 2007; Das and Baker, 2008; Zhou et al., 2008; Chen et al., 2010; Lasker et al., 2010).

Here, we describe an improved experimental and computational approach to determine the subunit configuration of macromolecular assemblies by computational integration of new kinds of biochemical and structural data. We apply this approach to the yeast Nup84 complex, defining the positions and relative orientations of the individual components. The resulting structure allows us to visualize structure–function relationships that provide insights into the assembly and evolution of the Nup84 complex and the NPC as a whole.

Results

Determination of macromolecular assembly structures by an integrative approach

Our approach involves (a) gathering of diverse and complementary experimental data, including data not typically used for structure determination, (b) representation of subunits and translation of the experimental data into spatial restraints on these subunits, (c) optimization by satisfaction of the spatial restraints to produce an ensemble of structures of defined precision and consistent with the data, and (d) analysis and assessment of the ensemble (Alber et al., 2007a,b, 2008; Lasker et al., 2010). We previously demonstrated this approach by determining the yeast NPC's molecular architecture based on a diverse set of proteomic and biophysical data. This map defines the approximate positions of the component proteins but not their shape or orientations (Alber et al., 2007a,b). We have now significantly enhanced our approach to allow us to easily integrate data spanning the scale from angstroms to hundreds of nanometers, greatly increasing fidelity and reliability of our mapping procedure. Here, we determine the positions and orientations of the subunits in the yeast Nup84 complex, using data from negative-stain EM, affinity purification and domain mapping, and x-ray structures and comparative models of subunits. The advantages of our approach are as follows: (a) precision, accuracy, and completeness of a structure are maximized by benefiting from the combination of varied datasets; (b) this precision and accuracy can be systematically assessed; and (c) efficiency is maximized by an iterative feedback between data collection and data processing.

Gathering data

We have used the two following primary methods to obtain a large quantity of structural information on the Nup84 complex.

Domain deletion mapping. Using domain boundary data (Devos et al., 2004; Dokudovskaya et al., 2006), we expressed domain-truncated nups constructed as in-frame chromosomal deletions under the control of their native promoters and C-terminally tagged with the Protein A (PrA) tag (see Materials and methods; Table S1). We determined the set of nups interacting with each of the tagged truncated nups by affinity purification and mass spectrometry (MS; Fig. 1). Purifications were adjusted so that we initially only probed interactions within the seven-protein complex (Table S1). The nups that are affinity purified with a truncated nup bait must necessarily interact (directly or indirectly) in vivo with the remaining domains (Fig. 2 A). Loss of an interaction is usually a result of the loss of a specific interaction domain; however, in rare instances, it can be a result of misfolding or mislocalization. For those truncations that caused a gross change in the interaction pattern, the tagged construct was analyzed by protease accessibility laddering
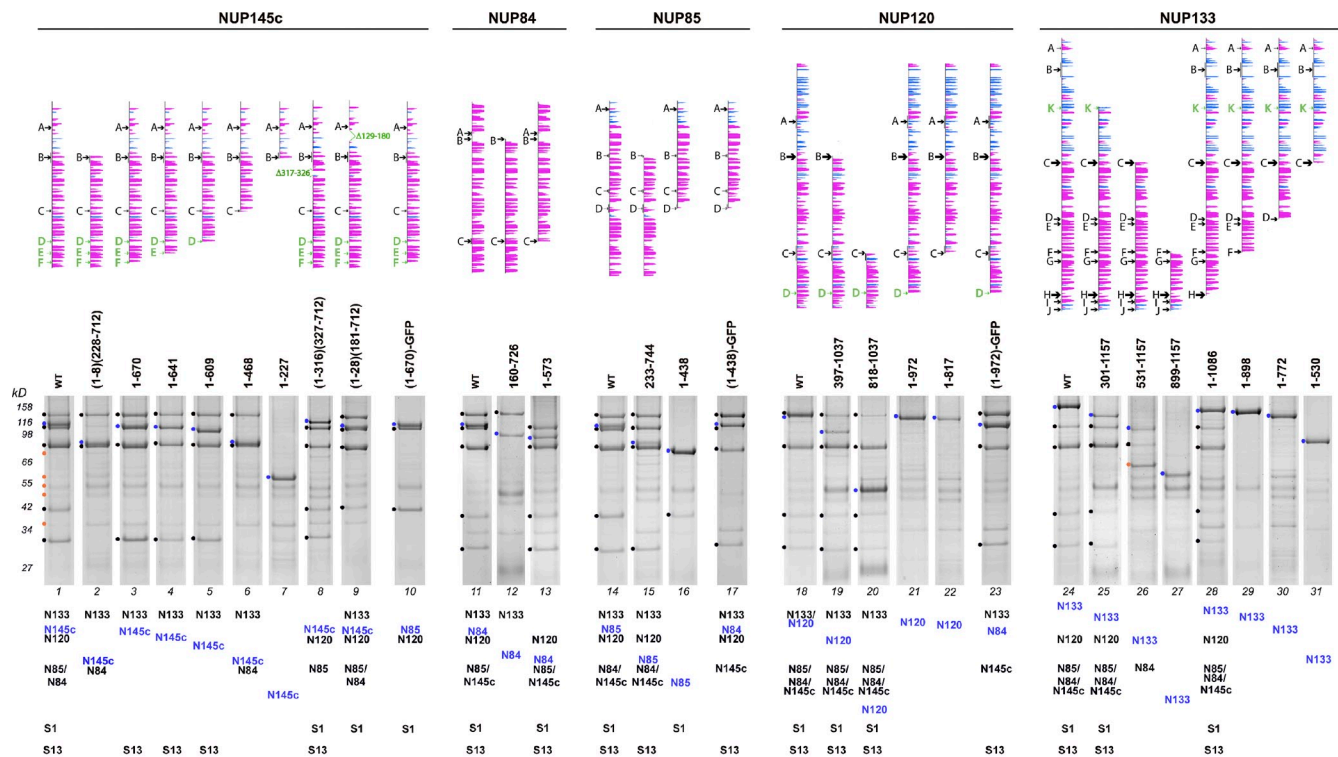
Figure 1. **Domain mapping of the Nup84 complex.** (top) Predicted secondary structure of truncated nup constructs. Vertical lines represent the sequence of each nup to scale, and secondary structure predictions are shown as horizontal bars of length proportional to the confidence of the prediction (α helices are shown in magenta and β-strands in cyan). PAL sites (Dokudovskaya et al., 2006) defining the limits of the truncations are indicated with arrowed black letters; truncation points selected by sequence alignment are indicated with arrowed green letters. (bottom) Coomassie-stained SDS-PAGE of affinity-purified PrA-tagged truncated Nup84 complex nups. Protein bands marked by filled circles at the left side of the gel lanes were identified by MS. The identity of the copurifying proteins is indicated in order below each lane (PrA-tagged nups are shown in blue, copurifying nups in black [N = Nup, S1 = Seh1, and S13 = Sec13], and contaminants in orange). WT, wild type.

(PAL; Dokudovskaya et al., 2006); in all cases, the PAL maps indicated that the remaining domains had folded correctly (unpublished data). All the truncations were also tested for their localization to the NPC in vivo (Fig. S1); mislocalization could have prevented a bona fide interaction from forming, and so no conclusion as to the loss of an interaction can be drawn in that case (Figs. 2 B and S1). However, if a truncation retained sufficient nup interaction regions to target it to the NPC, any lost interactions with the Nup84 complex components were taken as caused by the loss of the deleted domains, allowing us to map at least one interaction point to the deleted domain (Fig. 2 B).

EM. We used negative-stain EM to obtain the overall shape and dimensions of the affinity-purified Nup84 complex (Fig. 3). As expected, the observed particles exhibit a characteristic Y shape (Fig. 3 A; Lutzmann et al., 2002; Kampmann and Blobel, 2009). Other forms of the complex lacking Nup133 (Fig. 3 C; Siniossoglou et al., 2000) and a truncated version lacking Seh1 and the N terminus of Nup85 (Fig. 3 B) were also purified and analyzed to morphologically assign the compositional identity of the Y arms.

Representing and translating data into spatial restraints

Representation of the nups. Because few Nup84 complex components have full atomic resolution coverage, each nup was represented as a hybrid rigid body consisting of

its crystallographic data (if available), comparative models (if an accurate alignment could be computed), and/or a string of beads mimicking the coarse shape of a related known fold (Table 1); the minimum necessary number of structural modules was used in each case. 56% of residues in the Nup84 complex have been covered by the yeast crystallographic structures of individual domains (Hsia et al., 2007; Brohawn et al., 2008; Leksa et al., 2009; Sampathkumar et al., 2011). We modeled an additional 29% of residues based on alignments to related known structures (Table 1). Crystallographic interfaces have not been used in the initial modeling to allow the validation of the approach (see below and Fig. 6). However, this high-resolution information was used to generate an alternative ensemble (Fig. S2 C). Our previously determined stoichiometry for the complex (Rout et al., 2000) has since been corroborated (Lutzmann et al., 2002) and is used here, as was performed previously (Alber et al., 2007a,b).

Domain-mapping restraints. An affinity purification experiment produces a distinct set of coisolating proteins, which we term a composite; a composite may represent a single complex of physically interacting proteins or a mixture of such complexes overlapping at least at the tagged protein (Alber et al., 2007a). We previously described how to encode a composite as conditional connectivity restraints based on the proximities between the composite proteins (S_{dm}; see Materials and methods; Alber et al., 2005, 2007a,b, 2008). We still apply such

A

B
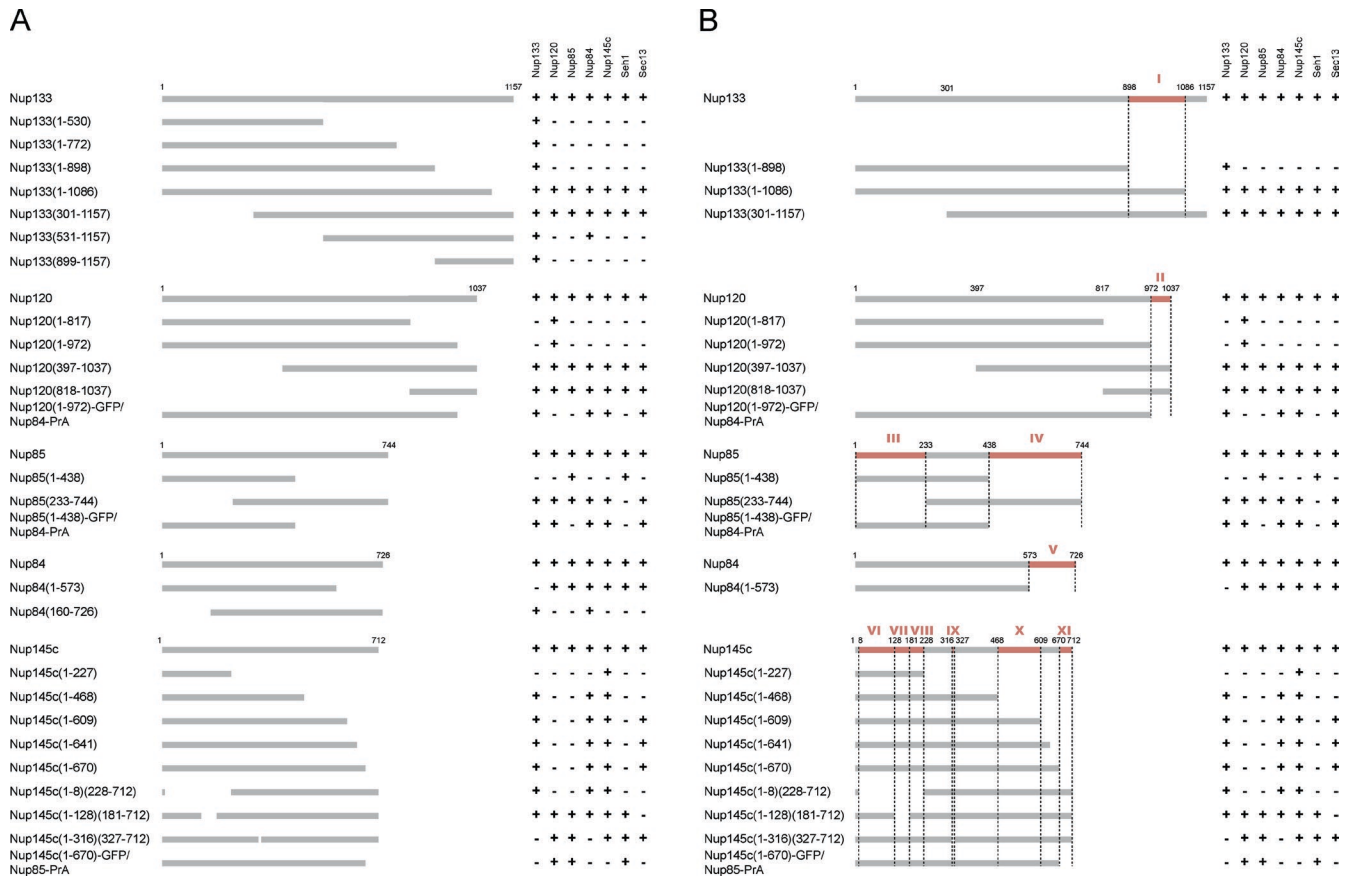
Figure 2.   **Identification of interacting regions within the Nup84 complex.** (A) Copurification profile of the different truncations analyzed. Horizontal gray lines represent the amino acid residue length of each protein and truncated version; amino acid residue positions are shown on top of the lines. On the right, MS-detected copurifying Nup84 complex nups are indicated (+), and undetected proteins are also indicated (−; see Table S3 for details). (B) Domain mapping. Truncations showing both nuclear rim localization by immunofluorescence and PAL profile consistent with proper folding were used to interpret a lost interaction as caused by the loss of at least one interaction point present in the deleted nup region (represented by red lines on the wild-type line). Each region is identified by red roman numbers. The identified interactions are as follows: Nup133 Region I interacts with Nup120, Nup145c, Nup85, Nup84, Seh1, and Sec13; Nup120 Region II interacts with Nup133, Nup145c, Nup85, Nup84, Seh1, and Sec13; Nup85 Region III interacts with Seh1; Nup85 Region IV interacts with Nup133, Nup120, Nup145c, Nup84, and Sec13; Nup84 Region V interacts with Nup133, Nup120, Nup145c, Nup85, Seh1, and Sec13; Nup145c Region VI interacts with Nup120, Nup85, and Seh1; Nup145c Region VII interacts with Sec13; Nup145c Region VIII interacts with Nup120, Nup85, and Seh1; Nup145c Region IX interacts with Nup133 and Nup84; Nup145c Region X interacts with Sec13; and Nup145c Region XI interacts with Nup120, Nup85, and Seh1.

conditional connectivity restraints here but now restrain positions of domains and protein fragments instead of whole proteins, thus orienting as well as localizing protein subunits (see the Domain deletion mapping section and Materials and methods).

   EM restraints. We constructed a class average of 2D EM images of the full Nup84 complex (Fig. 3 A) and used this class average to define a restraint and two filters (see Materials and methods) as follows. We first measured the dimensions of the class average of the full complex to define a bounding triangle restraint on the Nup84 complex (S_{tri}; see Materials and methods). Then, the class average of the full complex was also used as a filter on optimized models (S_{em}; see the Sampling good-scoring structures section and Materials and methods). Next, the class average for the six-member complex, missing Nup133 (Fig. 3 C), was also used as a filter in the same manner but compared with the portion of our structures containing the remaining six proteins (Nup84, Nup145c, Sec13, Nup85, Seh1, and Nup120). Finally, a filter was used to remove structures in which the longest arm of the complex (as measured by distance

from the bottom of the stem) incorrectly contained Nup85 and Seh1 rather than Nup120, as shown by the deletion class average (Fig. 3 B).

   Geometric complementarity and excluded volume. A low-resolution geometric complementarity term S_{acc} was included in our scoring function to reward shape complementarity and penalize steric clashes (Lasker et al., 2009).

Sampling good-scoring structures
Models that satisfied all the aforementioned restraints were obtained in four stages (see Materials and methods; Fig. 4). In the first, the coarse stage, 100,000 coarse models were calculated by a Monte Carlo optimization of the sum of S_{dm} and S_{tri}, each starting from a different random initial configuration. In the second, the refinement stage, the models were refined by a Monte Carlo optimization of the sum of S_{acc}, S_{dm}, and S_{tri}, with smaller step sizes. In the third, the filtering stage, the 10,000 top-scoring models were filtered by requiring sufficiently good alignment to the class averages of the EM images of the full and
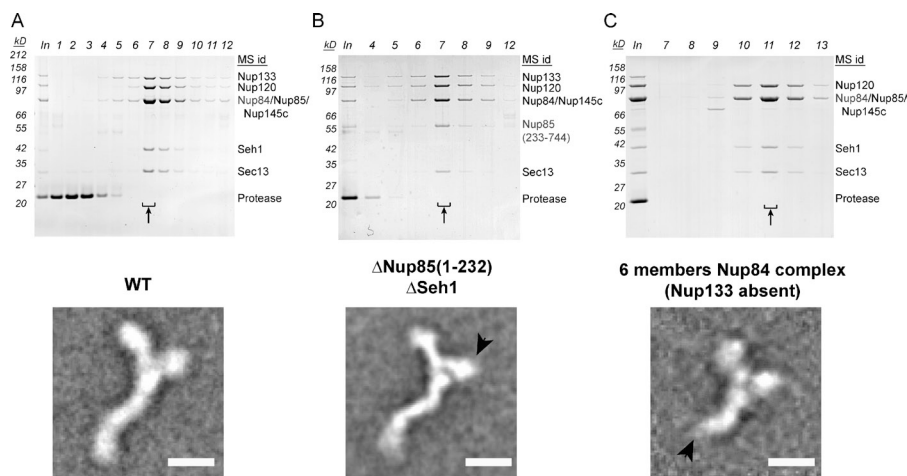
Figure 3. EM analysis of the Nup84 complex. (A–C) Affinity-purified Nup84 complexes corresponding to the full-length complex (A), Nup85(233–744) truncation (B), and the Nup84 complex lacking Nup133 (C) were purified by either sucrose gradient (A and B) or size-exclusion chromatography (C). Coomassie-stained SDS-PAGE of the precipitated input (In) and collected fractions are shown. Fractions indicated with arrows were analyzed by negative-stain EM. Class averages for each complex are shown in the bottom part of each panel. The missing mass observed in Nup85(233–744) truncation (B) and the six-member complex (C) are indicated with arrow-heads. WT, wild type. Bars, 10 nm.

partial complex (Fig. 3, A and C), eliminating 521 structures. Finally, the remaining 9,479 structures were relaxed by optimizing the sum of S_{acc}, S_{dm}, S_{tri}, and S_{em} using the simplex algorithm (Nelder and Mead, 1965).

Analyzing and assessing the ensemble of structures

The resulting 9,479 good-scoring models were clustered according to pair-wise C-α root mean square deviation (RMSD) and showed a single dominant cluster of solutions (Figs. 4 and 5). The average RMSD from the center of the cluster is 1.5 nm. Random subsets of 10% of the models also form a single dominant cluster with the average RMSDs from the center of the cluster of 1.4–1.6 nm. Thus, the precision of the ensemble does not significantly change even if only a small fraction of the good-scoring solutions are used, demonstrating that our optimization procedure is likely to have exhaustively sampled the set of possible solutions, given the data. The variability in the ensemble of good-scoring structures may reflect the heterogeneity (e.g., flexibility) of the sample as well as the lack of information to determine a highly precise structure.

We assess our models using the following six criteria (Alber et al., 2007a,b). First, our structures satisfy all the input restraints, even though the data were generated by disparate experiments. Second, all the data can be satisfied by a single cluster of structures at a resolution sufficient to determine domain–domain

Table 1. **Representation of each Nup84 complex protein**

Nup	Representation	Start residue number	End residue number	Target–template sequence identity	PDB accession no.	Template PDB accession no.
				%		
Nup84	Crystal	7	442		3iko	
	Gap	443	461			
	Model	462	723	15		2zct
				19		3cqg
				19		3cqc
	Gap	724	726			
Nup133	Gap	1	62			
	Model	63	481	16		1xks
	Gap	482	494			
	Model	495	879	15		3i4r
	Gap	880	945			
	Crystal	946	1,157		3kfo	
Nup85	Crystal	1	564		3ewe	
	Gap	565	604			
	Model	605	744			
Nup120	Crystal	1	729		3hxr	
	Spheres	730	1,029			
Nup145c	Model	25	129	19		3ez1
	Crystal	130	552		3bg0	
	Model	553	712	15		1w07
				29		3cmu

Crystal refers to using an x-ray structure from the PDB, Gap refers to an amino acid residue segment represented by spheres, and Model refers to a segment represented by an atomic comparative model. PDB codes are indicated for crystal structures used directly. PDB codes for templates and sequence identities for target–template alignments are indicated where comparative models were used to represent a fragment.
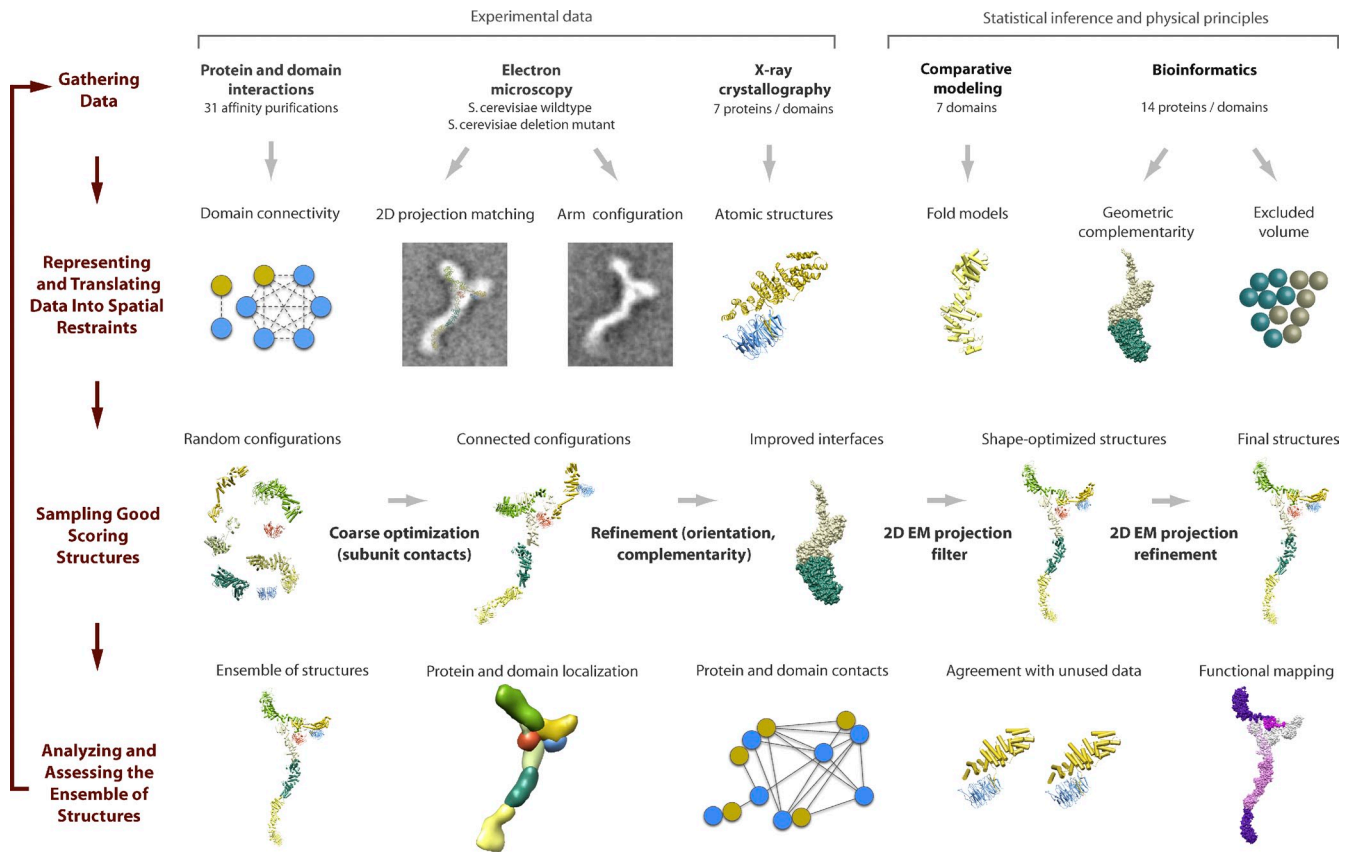
Figure 4. **Integrative structure determination of the Nup84 complex.** First, structural data are generated by experiments and computational methods. Second, the system is represented by mostly atomic structures of the subunits, and the data are translated into spatial restraints. Third, an ensemble of structures that satisfies the data is obtained by minimizing violations of the spatial restraints, starting from many different random configurations. Fourth, the ensemble is clustered into distinct sets of structures on the basis of similarities and analyzed in terms of geometry and accuracy.

interactions; this demonstrates that the sum of our data has a low level of ambiguity. Third, the ensemble is consistent with the structural data not used to compute it. For example, it recapitulates the three heterodimeric interfaces determined by crystallography (Hsia et al., 2007; Brohawn et al., 2008; Debler et al., 2008; Brohawn and Schwartz, 2009; Nagy et al., 2009), albeit at a lower resolution (15 Å). Among the solutions in our ensemble, a small number closely mimics the native interfaces, with a C-α RMSD <5 Å relative to the native state (Fig. 6 A), demonstrating that correct high-resolution solutions exist within our ensemble. Where available, we also compared the localization maps for interfaces generated in our 1.5-nm precision

ensemble with simulated maps of crystal dimers at a 1.5-nm resolution (Fig. S2 D), showing that our structure is consistent with available data at our defined precision. Fourth, a comparable ensemble is generated when random subsets of 10% of the data are removed (see Materials and methods), demonstrating the redundancy and correctness of the data as well as the structural ensemble. Fifth, the phenotypic data map onto the structure in a manner that is not expected by chance (see the Structure–function mapping of the Nup84 complex section). Sixth, we also computed the structure of the Nup84 complex by treating the three crystallographic dimers (see the third point in this section) as rigid bodies while again satisfying spatial

Figure 5. **Density map for the Nup84 complex ensemble.** (A) Two views of the localization density map are shown for the ensemble. The gray outer envelope represents the density within which 90% of all Nup84 complex structures in the final ensemble were localized, and the colored inner envelope was thresholded by visual inspection (to a volume containing 37% of ensemble density) to match the volume of an individual structure (also see Video 1). A few example structures that best fit the inner envelope according to 3D cross-correlation score and have among the lowest C-α RMSDs from the average structure comprised   of   the   9,479   final   good-scoring   solutions   are shown. (B) Two views of the density map, containing two fitted ribbon structures from the ensemble.
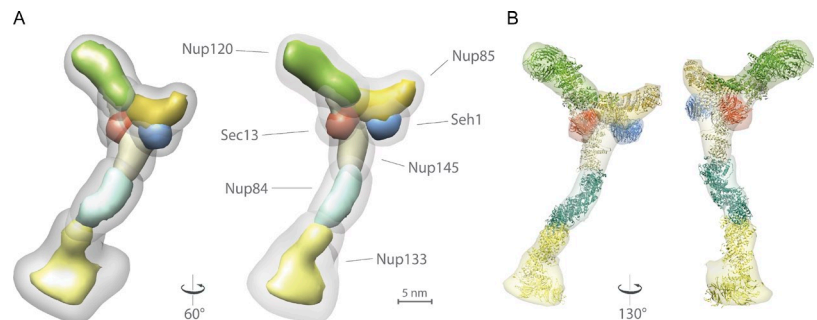
restraints implied by our own data (Fig. S2 C). As a result, the precision of the ensemble of the Nup84 complex improved from 1.5 to 1.1 nm without altering the molecular architecture of the complex. The most significant increase in the precision occurred for the β-propeller proteins Sec13 and Seh1 (Fig. S2 C), located closer to each other in the new ensemble. Although our biochemical analysis was not able to detect a direct interaction between these two proteins, we cannot exclude the possibility of interaction between them within the Nup84 complex structure. Further detailed analysis should be able to address this possibility.

Discussion

Structural features of the Nup84 complex

In agreement with previous work (Siniossoglou et al., 2000; Lutzmann et al., 2002; Kampmann and Blobel, 2009), the Nup84 complex structure is arranged in the shape of the letter Y (Fig. 5). The complex is composed almost exclusively of α-solenoid and β-propeller domains, with the majority of intersubunit interactions occurring through the α-solenoid domains (Fig. 6 B). Although we have used the available crystal structures of individual subunits to calculate the Nup84 complex structure here, at this resolution, representing all of the components with only homology models does not cause significant changes to the overall ensemble structure (Fig. S2 A). The degree of uncertainty in the localization of domains within the ensemble is shown in Fig. 5. Despite the map being of moderate precision, key features of interest are nevertheless revealed, including domain and fold-type arrangements as well as nup orientations and interactions.

The longer of the two short arms is entirely filled by Nup120, which is oriented with its β-propeller forming the tip of the arm and the α-solenoid forming the main body, the C-terminal region of which connects to the hub (Figs. 5 and 6). The α-solenoid region of Nup120 must form a single extended span along most of the length of the arm to connect the β-propeller of Nup120 to the rest of the complex. We used spheres to represent this region in the structure calculation. Such an extended α-solenoid is seen in the paralog of Nup120, Nup133, and so we have used a portion of Nup133 to represent these residues (Figs. 4–8; Whittle and Schwartz, 2009). Disconnecting Nup120 from the Nup84 complex does not lead to its release from the NPC (Fig. S1), indicating that Nup120 also directly interacts with nups outside the Nup84 complex. Indeed, it has been shown that Nup157 can connect in vitro to the Nup84 complex in a Nup120-dependent fashion (Lutzmann et al., 2005).

The other short arm is formed by Nup85 and Seh1 (Figs. 5 and 6). Our structure is consistent with crystal structures from a Nup85 fragment showing extensive contacts between the β-sheet N-terminal blade of Nup85 with a cognate groove in Seh1 as well as between Seh1 loops and N-terminal residues of Nup85 (Fig. 6, A and D; Brohawn et al., 2008; Debler et al., 2008). The C-terminal portion of Nup85 forms the hub connection (Fig. 6), and deletions in this region cause loss of both Nup85 and Seh1 from the complex (Fig. 1). Previous fittings of crystal structures to an EM density map of the Nup84 complex (Kampmann and Blobel, 2009; Nagy et al., 2009) have the Nup85/Seh1 dimer
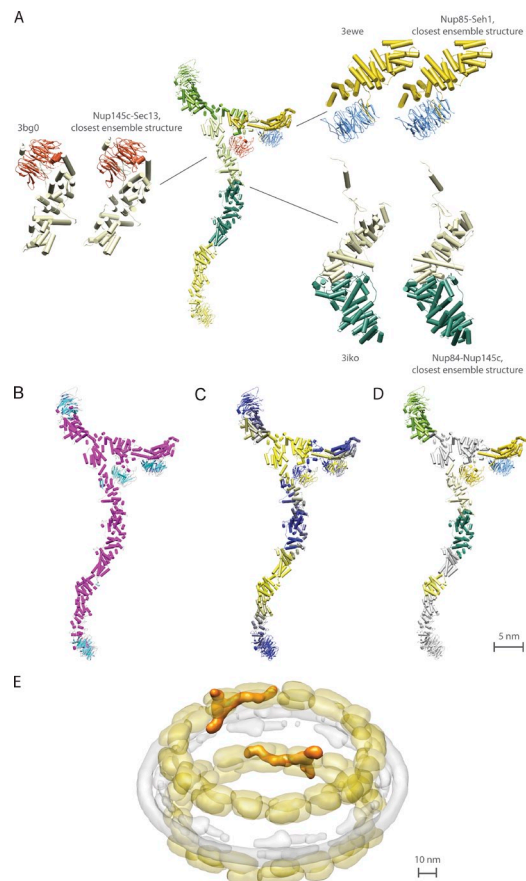
Figure 6. **Structural features of the Nup84 complex.** (A) Comparison of protein–protein interfaces in our ensemble with crystallographically determined interfaces. Atomic structures for the Nup85-Seh1 (NCBI Protein Data Bank accession no. 3ewe; Brohawn et al., 2008), Nup145c-Sec13 (PDB accession no. 3bg0; Hsia et al., 2007), and Nup84-Nup145c (PDB accession no. 3iko; Nagy et al., 2009) interfaces are shown alongside the best recapitulation of each interface found among the 9,479 ensemble structures, in which the best interface has the lowest RMSD between the dimer in the model and a crystal structure of the same dimer. A single full Nup84 complex structure is provided for reference. (B) Secondary structure elements. Helical regions (α-solenoids) are shown in pink. Sheet regions (β-propellers) are shown in cyan. (C) Indication of the N and C termini positions. Each of the Nup84 complex proteins is graded from its N terminus (blue) to the C terminus (yellow). (D) Crystal structure coverage. Where crystal structures were used to represent components of the Nup84 complex structure, the complex is colored; where atomic comparative models were used, fragments are shown in gray. (E) The density of a representative Nup84 complex structure was fitted into our previously published NPC map (Alber et al., 2007b) based on the relative positions of each component within the map. One of eight instances of the structure in each of the two outer rings of the complex is shown.

oriented in a manner inconsistent with our domain mapping and structure. However, the EM map used for these fittings is entirely consistent with our structure (Fig. S2 B), showing how integration of diverse data sources (here domain mapping and EM) can improve the accuracy of structure determinations. It has been shown that under crystal-packing conditions, the N terminus of Nup85 and Seh1 generates an extensive interaction surface used to connect it with another Nup85-Seh1 dimer (Debler et al., 2008). We found no evidence in our data for such a connection in vivo. However, the orientation of the Nup85-Seh1 dimer in our structure, facing outwards on its arm, allows us to suggest

that the crystal-packing interaction surface may actually be used by the Nup84 complex to connect to other Nups of the NPC core. This is also consistent with our identification of Nup85 and Seh1 as hotspots for fitness and connectivity in our map (see the Structure–function mapping of the Nup84 complex section).

The two short arms connect to the main stalk of the complex through a hub where an intricate interaction is established. There are no published atomic structures for this interface, but we determined that this hub is formed by the C-terminal extremes of three different α-solenoids (Nup85, Nup120, and Nup145c) and the N terminus of Nup145c (Fig. 6 B). Though this N-terminal Nup145c region has been predicted to be disordered (Hsia et al., 2007), it actually appears to be a part of the structured hub region and is essential for maintaining the connection between the short arms and the long stalk in vivo. The precision of the ensemble does not allow us to define the exact interaction surfaces comprising the hub.

Although located near the hub (Fig. 6), Sec13 is not required for the arms–stalk connection to form (also see Figs. 1 and 2 A). Similarly, the β-propeller protein Seh1 is also not required for the formation of the hub. The α-solenoid of Nup145c forms the upper part of the stalk, connecting through its middle region to Nup84, as has been previously described (Fig. 6; Brohawn and Schwartz, 2009; Nagy et al., 2009). However, our data do not support a suggested homodimerization of Nup145c (Hsia et al., 2007), as the putative dimerization region instead forms a connection to Nup84, agreeing with several published crystal structures (Brohawn and Schwartz, 2009; Nagy et al., 2009) and point mutants (Brohawn et al., 2008). In our ensemble, the N- and C-terminal regions of Nup145c connect directly with the Sec13 β-propeller (Fig. 6); domain-mapping data show that both regions of Nup145c are required, but neither is individually sufficient, for a stable Sec13–Nup145c interaction (Fig. 2 B), agreeing with previous data (Hsia et al., 2007).

The Nup84 α-solenoid forms the middle part of the stalk (Figs. 5 and 6), connecting to Nup145c through its N-terminal region (Fig. 6 C). Nup133 and Nup84 connect through the C-terminal end of their α-solenoid domains (Fig. 6) in a tail-to-tail fashion that has been previously seen in their human homologs (Boehmer et al., 2008). The fact that certain Nup133 mutants that are unable to interact efficiently with Nup84 nevertheless localize to the NPC (Fig. S1) suggests that proper localization of yeast Nup133 to the NPC is not exclusively driven by its interaction with Nup84 (seemingly unlike its human counterpart; Boehmer et al., 2003, 2008).

Position of the Nup84 complex in the NPC

Our NPC map (Alber et al., 2007b) positioned two sets of eight copies of the Nup84 complex arranged to form the two outer rings of the NPC. The structure of the Nup84 complex described in the present study is entirely consistent with this arrangement (Fig. 6 E), although none of the data used in the determination of the original NPC map was used in the present Nup84 complex calculation. A fencelike model based on crystallographic homodimeric contacts (discussed in the Structural features of the Nup84 complex section; Debler et al., 2008) is incompatible with the arrangement of interfaces shown in our structure.

Alternatively, a vertical arrangement for the Nup84 complex has been postulated (Brohawn et al., 2008). Although our data do not exclude variants of this possibility, alignment of our new data with our previous map points to a horizontal head-to-tail arrangement of the Nup84 complex to comprise the NPC's outer rings (Fig. 6 E). A recent fluorescence anisotropy study (Kampmann et al., 2011) defines the orientation of the human Nup107-Nup133 dimer as being parallel to the NE plane, which is in agreement with our arrangement for its yeast counterpart.

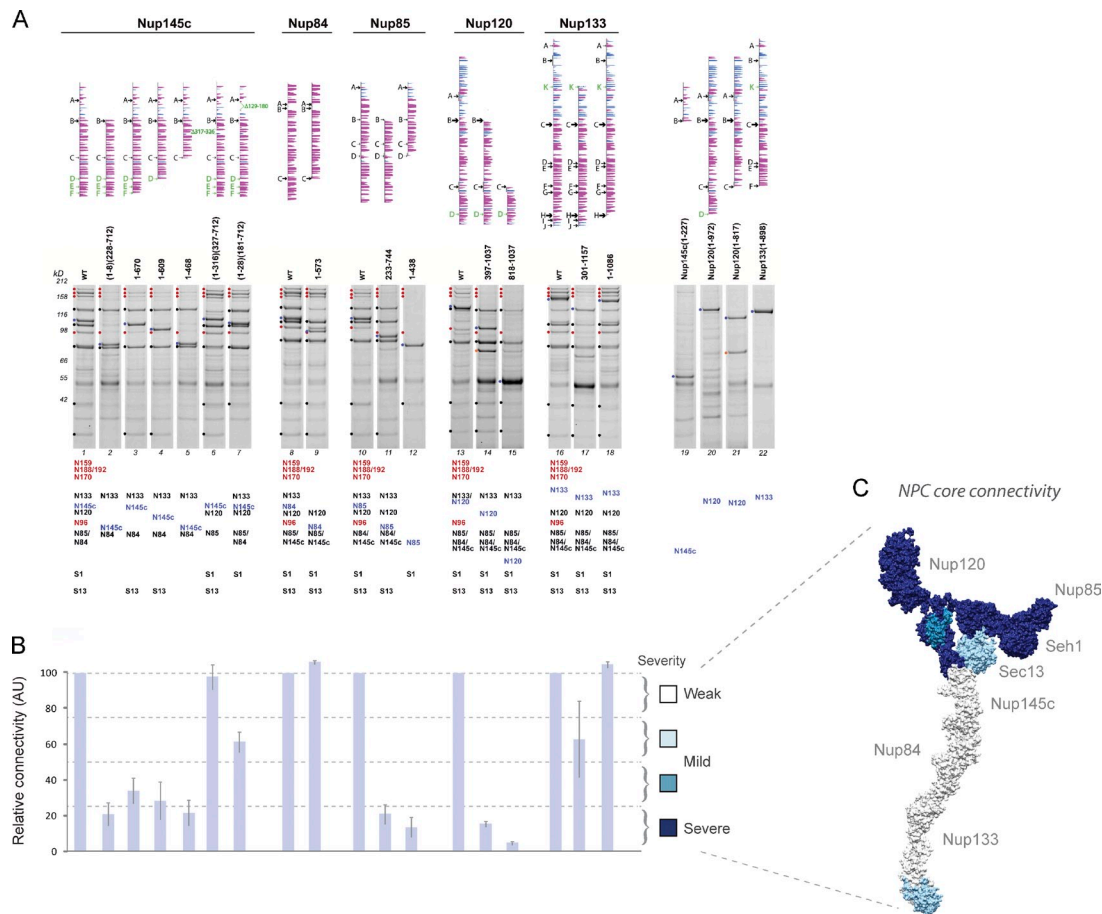### Mapping the connectivity of the Nup84 complex within the NPC

It is still not known exactly how the Nup84 complex connects to the rest of the NPC, though it seems to be a stable rather than dynamic interaction (Dultz et al., 2008). One possibility is that a stable connection could be formed through a few strong heterodimeric interactions to key neighboring Nups of the same character that hold the Nup84 complex itself together; alternatively, the complex may be held to the rest of the NPC through multiple relatively weak, cooperative interactions (Amlacher et al., 2011). To define the nature of the Nup84 complex connectivity, we have analyzed the stability of the connection between the Nup84 complex and several NPC core components using our set of truncation mutants. We affinity purified the Nup84 complex under conditions that copurify nups forming the core of the NPC (Fig. 7 A; Alber et al., 2007b) in all the mutants that showed proper NPC localization (Fig. S1). We quantified the signal obtained in the gels for five NPC core nups (inner ring nups Nup192, Nup188, and Nup170, linker nup Nic96, and cytoplasmic side nup Nup159; Fig. 7 B). Mutants that showed no connection to other components of the Nup84 complex were considered not informative and were not used for quantification (Fig. 7 A, right). These measurements were then converted into a heat map, revealing regions involved in the connection between the Nup84 complex and the analyzed core nups (Fig. 7 C).

Truncations that affect the short arms and the hub ablate copurification of core nups with the Nup84 complex, whereas truncations in most other regions of the Nup84 complex have a lesser effect on interactions with the analyzed core nups (Fig. 7). β-Propeller proteins and domains seem to have a key role on the interaction pattern, consistent with their peripheral location in the Nup84 complex (see the Structure–function mapping of the Nup84 complex section).

Notably, although truncations in a given Nup84 complex protein cause the absolute loss of a very discrete subset of other Nup84 complex proteins, such deletions did not lead to the loss of discrete subsets of core Nups. Instead, deletions in the hotspots led to a varying degree of loss of all the core Nups simultaneously, whereas deletions elsewhere had little effect. This is inconsistent with the idea that there is a single or small number of discrete high-affinity interactions, analogous to those comprising the Nup84 complex itself, that hold the complex in the NPC. Rather, as seen recently with the Nic96 complex (Amlacher et al., 2011), the distribution and behavior of the hotspots show a pattern consistent with the Nup84 complex connecting through multiple relatively weak, cooperative interactions to the NPC core.

Figure 7. **Mapping the Nup84 complex connectivity to the NPC core.** (A) Predicted secondary structure of truncated nup constructs, as described in the Fig. 1 legend, are shown on the top. Coomassie-stained SDS-PAGE of affinity-purified PrA-tagged truncated Nup84 complex nups and copurifying NPC core nups are shown in the middle. Protein bands marked by filled circles at the left side of each gel lane were identified by MS. The identity of the copurifying proteins is indicated in order below each lane (PrA-tagged nups are shown in blue, Nup84 complex copurifying nups in black, NPC core copurifying nups in red, and contaminates in orange; N = Nup, S1 = Seh1, and S13 = Sec13). Lanes corresponding to truncations that show no connection to other Nup84 complex components are shown on the right and were not used for the analysis. WT, wild type. (B) Quantification of the relative connectivity to the NPC core of the Nup84 complex truncation mutants. A bar graph showing the average relative molar ratio of the copurified NPC core nups is shown (see Materials and methods for details). Bars show the average value for each mutant, and the error bars define the upper and lower values obtained. Each bar is aligned with its corresponding gel lane in A. Proportional divisions (dashed gray lanes) were made, and a color code was assigned to each division (right) from dark blue to white (colored squares) to match the increasing degree of connectivity. n = 2. AU, arbitrary unit. (C) A heat map reflecting the key regions for the connectivity of the Nup84 complex to the NPC core. The color code defined in B was used to generate a heat map using a single Nup84 complex structure from the ensemble.

The presence of such cooperative interactions between putative stable building blocks of the NPC (such as the Nup84 complex) might be necessary for the NPC assembly process, as it ensures that the core NPC would only be formed when all the building blocks are located together in a certain region of the NE, and would prevent these building blocks assembling prematurely elsewhere in the cell. In summary, these connectivity experiments support the idea that the short arms of the Nup84 complex are involved in establishing key cooperative contacts with the core components of the NPC.

Structure-function mapping of the Nup84 complex

An advantage of our approach is that the same constructs used for structural domain mapping can also generate phenotypic profiles for functional characterization of those same domains. Integrating both structural and phenotypic information is thus efficient,

allowing us to map the regions of the complex that fulfill relevant functional roles. We have analyzed two of the most characteristic phenotypes common to mutations in the Nup84 complex components: fitness (growth) and NPC clustering (Doye and Hurt, 1995; Fabre and Hurt, 1997). The different truncations displayed a wide range of phenotypic defects in both fitness (Fig. 8 A) and NPC clustering (Fig. 8 B) from mild to severe. To compare the severity of the different phenotypes in each strain, we performed semiquantitative measurements (see Materials and methods). These measurements were converted into heat maps of the Nup84 complex depicting the severity of the phenotypes (Figs. 9 and S3). The distribution of hotspots in the two phenotypic maps is nonrandom, forming distinct patterns in the structure.

Severe fitness phenotypes map strongly to the tips of the two short arms of the complex and, to a lesser extent, to the tip and middle region of the stalk (Fig. 9 A). The connectivity heat map shows strong similarities to the fitness phenotype heat map
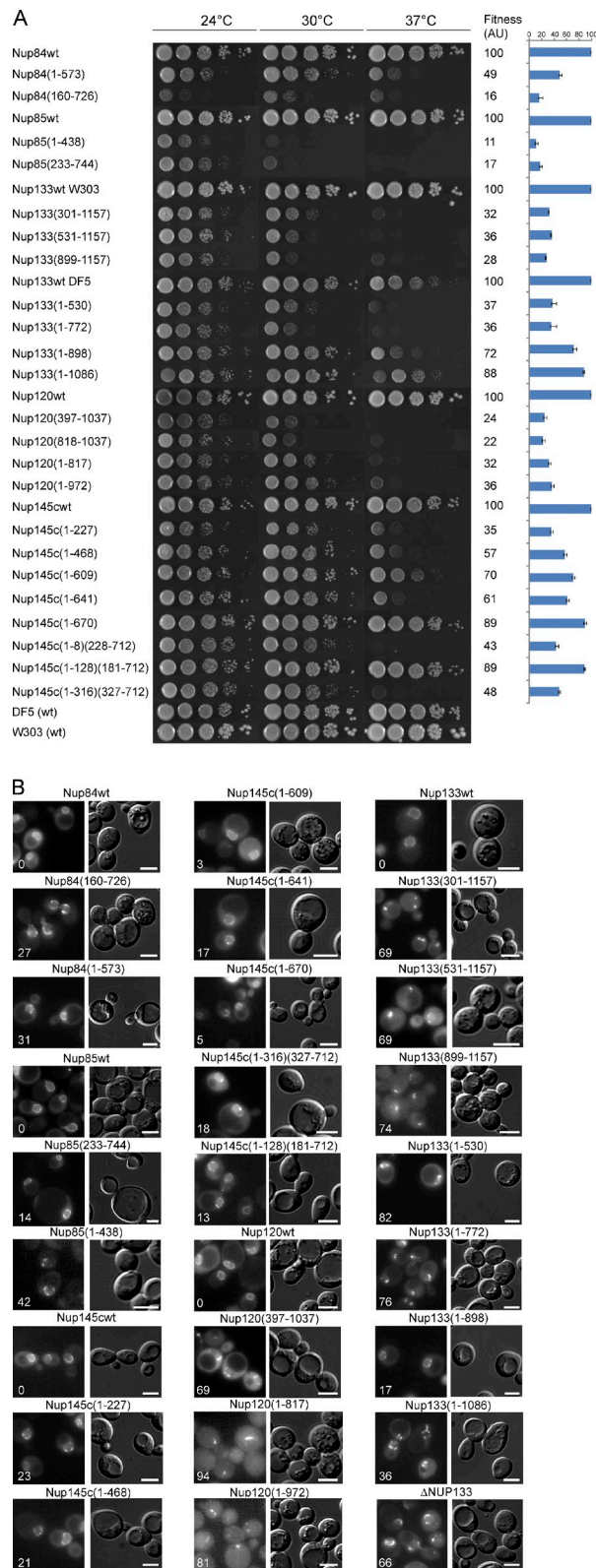
Figure 8. Fitness and NPC clustering analysis of the Nup84 complex truncations. (A) Growth tests at different temperatures (24, 30, and 37°C) for the full-length (wild type [wt]) and truncated versions of the Nup84 complex nups. Serial 10-fold dilutions of cells were spotted on YEPD plates and grown at the indicated temperatures for 1–3 d. Parental strains DF5 and w303 as well as the full-length genomically tagged Nup84 complex nups (Nup84, Nup85, Nup133, Nup120, and Nup145c) were included as controls. Each growing phenotype was quantified by semiquantitative

(compare Figs. 7 C and 9 A) but does not strongly resemble the heat map generated for the NPC clustering phenotype (Fig. 9 B), for which we propose a different molecular basis (see the next paragraph). Collectively, this suggests that the tips of the Nup84 complex are involved in connecting the complex to other components of the NPC scaffold—such as the inner rings and linker nups—and stabilizing the normal functional structure of the NPC's scaffold. Thus, a major reason for the strong fitness phenotypes observed is likely the loss of connectivity between the Nup84 complex and the NPC core, leading to a functionally compromised NPC.

The clustering phenotype hotspots map mainly to the Nup133 tip of the stalk and the Nup120 short arm (Fig. 9 B). Strikingly, truncations affecting the short arm component Nup85 do not exhibit such a marked clustered NPC distribution, which is in agreement with the observed low level of NPC clustering for *nup85* partial gene disruptions and a null allele of its dimeric partner Seh1 (Siniossoglou et al., 1996, 2000). The clustering hotspot-containing proteins Nup133 and Nup120 are known paralogs and resemble VCC proteins such as clathrin (Devos et al., 2004; Alber et al., 2007b). The NE is formed by two parallel membranes, the outer and inner nuclear membranes; at the outer rings, where we localize the Nup84 complex, these two membranes are deflected to form the pore membrane, which anchors the NPC in the NE (Yang et al., 1998; Stoffler et al., 2003; Beck et al., 2004; Alber et al., 2007b). Therefore, we hypothesize that the Nup84 complex and particularly the clathrin-like Nup120 and Nup133 are key proteins in ensuring the stability of the interface between the NPC and the surrounding outer and inner nuclear membranes. Clustered NPCs are known to result from the migration of preexisting NPCs into aggregates rather than from the assembly of new NPCs into a fixed site on the NE (Bucci and Wente, 1997). Furthermore, we suggest that clustering of NPCs can result from destabilizing the interface of the NE membranes with the Nup84 complex outer rings. Hence, we might expect an aggravation of the clustering phenotype were we to further destabilize the NE membranes. To test this hypothesis, we used benzyl alcohol (BA), a reagent that fluidizes and destabilizes membranes (Gordon et al., 1980) and which has been extensively used to investigate membrane dynamics and even membrane–NPC interactions in yeast and other fungi (Scarcelli et al., 2007; Liu et al., 2009; Titus et al., 2010). Although BA does not affect the stability of the purified Nup84 complex (Fig. S4), the degree of clustering in mutants was indeed aggravated by the treatment with BA, whereas a wild-type strain was

methods (see Materials and methods), and the obtained value (in arbitrary units [AU]) is shown on the right of each column. Plotted fitness value (mean ± SEM) for each measurement is shown on the right. (B) The left image of each column shows the localization of a Nup49p-CFP reporter in wild-type and truncation mutants as determined by fluorescence microscopy. A NUP133 gene deletion is also shown as a reference for NPC clustering (Belgareh and Doye, 1997). The right image of each column shows the differential interference contrast image of the same cells. The number shown on the bottom left corner of the fluorescence picture represents the measured degree of clustering for each strain (represented by their normalized CV, multiplied by 100 for representation purposes) in arbitrary units for n = 30 cells (see Materials and methods). Bars, 5 µm.
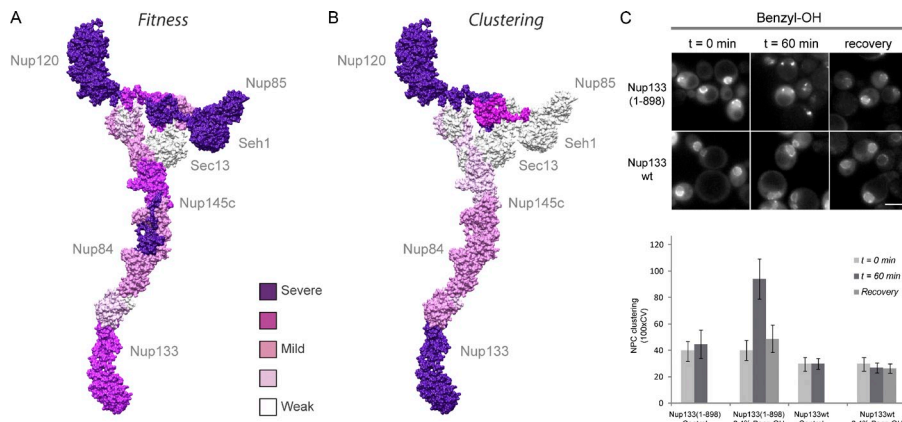
Figure 9. **Phenotypic heat maps of the Nup84 complex: Fitness relates with loss of interactions between the Nup84 complex and other core NPC nups, whereas NPC clustering is related to NE membrane stability.** (A and B) Effect of truncated regions of the Nup84 complex on organism fitness and NPC clustering. The severity of fitness phenotypes (A) and NPC clustering (B) for specific truncations of the Nup84 complex are shown mapped into a single Nup84 complex structure. The color code is shown in between the maps and in Fig. S3. (C) Membrane-destabilizing assay. 0.4% BA was added to wild-type (wt) or truncated mutant Nup133(1–898) (similar behavior was observed for other mutant strains; not depicted). The time course localization of fluorescent reporter Nup49-CFP after treatment and for nontreated controls is shown on the top. Quantification of the level of NPC clustering (see Materials and methods) for each time point is shown on the bottom (mean ± SD; n = 30). Bar, 5 µm.

not affected, with the BA-induced clustering being fully reversible (Fig. 9 C). These results support the hypothesis that the β-α nups Nup133 and Nup120 are directly contacting and/or helping in the stabilization of the curvature of the NPC membrane just as VCCs do.

With the α-solenoids forming the architectural core of the complex (Fig. 6 B), an obvious question arises: what is the function of the β-propeller domains? As previously mentioned, they do not appear to be structural keystones of the Nup84 complex. However, our functional data identify them as hotspots for structural integrity of the NPC, connectivity to the NPC core, and stabilization of the NE membrane (Figs. 8 and 9). Altogether, these data suggest that the β-propeller domains of the Nup84 complex are involved in NPC–NE membrane interactions and in connecting each Nup84 complex with neighboring complexes in the NPC. Precisely such a role for β-propeller domains in connecting complexes is found in COPI, COPII, and clathrin complexes (ter Haar et al., 2000; McMahon and Mills, 2004; Miele et al., 2004; Stagg et al., 2008; Lee and Goldberg, 2010).

Evolution of the Nup84 complex

The connections between Nup84 complex components are established mainly between the α-solenoid domains in two different fashions (Figs. 6 and 10; Hsia et al., 2007; Brohawn et al., 2008; Brohawn and Schwartz, 2009): first, tail to tail, as in the hub and Nup133–Nup84 connections, reminiscent of the COPI β'-cop and α-cop subunits and the clathrin triskelion arrangement, and second, the connection between the mid α-solenoid domain of Nup145c and the N-terminal head of Nup84, reminiscent of the dimeric connection between Sec31 units in COPII (Fotin et al., 2004; Fath et al., 2007; Lee and Goldberg, 2010). Thus, the Nup84 complex is an excellent exemplar for the protocoatomer hypothesis (Devos et al., 2004, 2006; Alber et al., 2007b; Field et al., 2011), having structural and connectivity features found in several of the VCCs and even sharing components with other vesicle-coating and -tethering complexes (Devos et al., 2004; Dokudovskaya et al., 2011).

We have previously suggested that the descent of the modern coatomer-like complexes from a single common ancestor occurred through the processes of duplication, divergence, specialization, and secondary loss (Devos et al., 2004, 2006; Alber et al., 2007a,b; Field et al., 2011). In the light of the present structure, we can speculate how evolution shaped the modern Nup84 complex (Fig. 10). A hypothetical duplication symmetry axis can be drawn between the interface of Nup84 and Nup145c, consistent with our previous data suggesting that each of the eight spokes in the NPC consists of two columns that arose from a genome duplication event and that the Nup84 complex spans both columns (Fig. 6 E; Alber et al., 2007a,b). On both sides of this axis, paralogous components can be found: the β-α paralogs Nup120/Nup133 and the α-solenoid paralogs Nup145c/Nup84. Crystal structures have shown that the connection between Nup145c and Nup84 is established through a similar U-turn region of their α-solenoids (Brohawn and Schwartz, 2009; Nagy et al., 2009). Both of their C-terminal domains reach back to connect through their C-terminal extremes to a β-α protein (Nup120 and Nup133, respectively; Fig. 10). Nup145c makes another connection involving the C terminus of Nup85, forming a triskelion-like structure that can be reconstituted in vitro (Lutzmann et al., 2002). We suggest that originally, two triskelion-like subcomplexes were connected through their Nup145c-Nup84 homologs (Fig. 10). The current Nup84 complex architecture would have been generated by the simple loss of a hypothetical N-terminal region of the Nup84 ancestor protein and its associated hypothetical Nup85-like protein. The conservation of many of the Nups comprising the Nup84 complex between highly divergent branches of the eukaryotic evolutionary tree (DeGrasse et al., 2009) suggests that this duplication-loss scenario occurred near or even before the root of the eukaryotic tree. In this proposed duplication scheme, we note that the functional hotspots detected in our analysis are surprisingly well-symmetrically located, with the functional hotspots mainly mapping to the boundaries between the duplicate columns and spokes (Fig. 6 E; Alber et al., 2007b). Yet, more ancient duplications can be envisioned from the structural similarity between
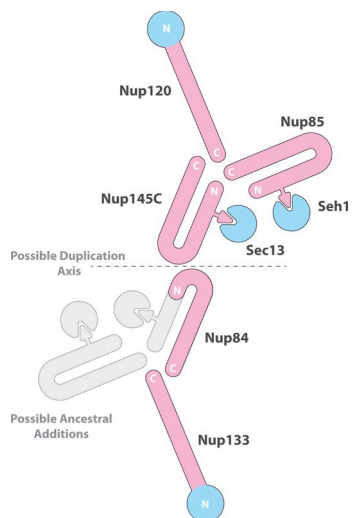
Figure 10. **Potential origin of the Nup84 complex through ancient gene duplications and losses.** A diagram of the Nup84 complex nup arrangement is shown. β-propeller domains are colored in cyan, α-solenoid domains are colored in magenta, and invasion domains (Hsia et al., 2007; Brohawn et al., 2008) are indicated with magenta arrows. The N- and C-terminal ends of each protein are highlighted. The hypothetical duplication axis is shown as a dashed gray line dividing the complex between the Nup145c and Nup84 interaction surfaces. Possible ancestral nups lost after the duplication are shown as faded gray domains.

the paralogous components Nup85 and Nup145c and their paralogous partners Seh1 and Sec13, respectively.

Whereas COPI, COPII, and clathrin building blocks arrange in symmetrical homooligomers to form cages that coat membrane vesicles, similar building blocks arrange in asymmetrical heterooligomers to form the Nup84 complex (Fig. 6). We suggest that this kind of heterooligomeric arrangement evolved through duplication and divergence, as suggested in this section, to prevent the Nup84 complex coat from oligomerizing into a continuous cage. Instead, heterooligomerization (with one monomer being in this respect monofunctional) ensures that the region of membrane coated by the NPC is sharply limited, both radially and vertically, forming a circumscribed macromolecular structure of the correct size and morphology to form a discrete, precise macromolecular channel.

Materials and methods

Yeast strains and materials
All yeast strains used in this study are listed in Table S2. Strains were grown at 30°C in YPD media (1% yeast extract, 2% bactopeptone, and 2% glucose), except for the thermosensitive strains that were grown at 25°C in the same media. The following materials were used in this study: Dynabeads M-270 Epoxy (143.02D; Invitrogen); rabbit IgG (55944; MP Biomedicals); protease inhibitor cocktail (P-8340; Sigma-Aldrich); Asp-N, Lys-C, and trypsin (11420488001, 11420429001, and 11418025001; Roche); HRP-rabbit IgG (011–0303-003; Jackson ImmunoResearch Laboratories, Inc.); anti-GFP antibody (11814460001; Roche); anti–mouse IgG-HRP (NA931V; GE Healthcare); and Solution P (2 mg Pepstatin A, 90 mg PMSF, and 5 ml of absolute ethanol).

Domain mapping of the Nup84 complex
Domains forming the Nup84 complex nups were dissected by C- and N-terminal genomic truncation and PrA tagging so that each domain was expressed under the control of its native promoter. Points of truncation for each nup were selected based on the protease-sensitive amino acids

described by the PAL technique in Devos et al. (2004) and Dokudovskaya et al. (2006). Many of the cleavage sites had been narrowed to a single amino acid residue, and these served as the deletion sites; otherwise, the point of deletion was selected as the midpoint of the corresponding disordered region (Devos et al., 2004). Some deletions were also designed to eliminate conserved regions identified by multiple sequence alignment and secondary structure prediction (Devos et al., 2004). The C-terminal deletions were constructed by in-frame integration of a PCR-derived DNA fragment encoding flanking gene-specific sequences (45 nucleotides) and the IgG-binding domains of *Staphylococcus aureus* PrA amplified from the plasmid pProtA/HIS5, which carries the *Schizosaccharomyces pombe HIS5* gene as its selectable marker (Rout et al., 2000). Positive colonies were selected on synthetic complete medium lacking histidine. Internal and N-terminal deletions were constructed using the Cre–Lox P recombination system, as previously described (Gueldener et al., 2002; Strawn et al., 2004). In brief, a PCR-derived DNA cassette, encoding gene-specific overhanging sequences (45 nucleotides), and the *Kluyveromyces lactis LEU2* gene marker, flanked by LoxP sequences, were amplified from the plasmid pUG73 (EUROSCARF). The cassette was used to transform a strain in which the target nup was already PrA tagged (Rout et al., 2000). During the PCR, the first LoxP sequence of the cassette was modified to maintain the correct reading frame of the nup by modification of the vector-specific sequence in the original 5′ oligonucleotide (5′-GCCAGCAGAAGCTTCGTACGC-3′; Gueldener et al., 2002). Cre-recombinase expression was used to remove the selection marker in positive clones. Tetrads were dissected to obtain haploid strains carrying the mutant copy of the nup when diploid strains were used for the construction. Proper integration was tested by sequencing, and the constructs found to be stably expressed by Western blot analysis were analyzed (Table S1).

The NUP145 gene is transcribed as a precursor polypeptide that is posttranslationally self-cleaved to produce two independent peptides, Nup145n and Nup145c (Teixeira et al., 1999). To ensure that the expression of each of our Nup145c deletions was controlled by its native promoter, they were designed to retain the target region of the self-catalyzed cleavage between NUP145n and NUP145c (first nine amino acids of N145c), and their ability to undergo self-cleavage was tested by inmunoblot analysis. C-terminal tagging and truncations of Nup85 and Nup120 using the GFP tag were performed essentially as described above for the PrA-tagged versions using a PCR-derived DNA fragment encoding the GFP protein and the *Escherichia coli kanr* Geneticin/G418 resistance gene, amplified from the plasmid pFA6-GFP-kanMX6 (Longtine et al., 1998). Truncated mutants were crossed with strains expressing the wild-type copy of Nup84 tagged either with PrA or the ppx-PrA version (see the Purification of native Nup84 complexes section) to obtain strains carrying a combination of the GFP-tagged truncated nup and a PrA-tagged version of a wild-type Nup84 complex nup.

All mutant strains were analyzed by immunofluorescence as previously described (Wente et al., 1992) to analyze the subcellular localization of the PrA-tagged truncated nups (Fig. S1). Cells were grown to early log phase and then fixed with 4% formaldehyde in phosphate buffer for 5 min. Fixed cells were washed with 1.2 M sorbitol-phosphate buffer and spheroplasted using 10% glusulase (DuPont) and 1 mg/ml Zymolyase 20T (Seikagaku Corporation). Spheroplasts were immobilized into polylysine-coated slides and dehydrated by sequential immersion in cold methanol and acetone. Cells were blocked with 2% powdered nonfat milk in TBS buffer for 10 min at room temperature. Primary antibody (1:300 of rabbit affinity-purified antibody to mouse IgG; MP Biomedicals) and secondary antibody (Alexa Fluor 568–conjugated donkey anti–rabbit IgG (H + L); Invitrogen) were diluted in blocking solution and incubated overnight at 4°C and for 1 h at room temperature, respectively. Cells were mounted (100 mg/ml p-phenylenediamine in PBS with 0.05 µg/ml DAPI) and visualized at room temperature with a 63× 1.4 NA Plan-Apochromat objective (Carl Zeiss) using a microscope (Axioplan 2; Carl Zeiss) equipped with a cooled charge-coupled device camera (ORCA-ER; Hamamatsu Photonics). The system was controlled with Openlab imaging software (PerkinElmer). Final images were assembled, and γ-levels were adjusted to enhance contrast only using Photoshop software (Adobe).

To analyze the proteins interacting with the wild-type nup and each truncated construct, we followed the affinity purification procedure described previously by our groups (Alber et al., 2007a; Oeffinger et al., 2007). In brief, liquid nitrogen–frozen yeast cells were cryogenically broken using a planetary ball mill (Retsch GmbH). Frozen powder was resuspended in immunopurification buffer and incubated for 30 min with IgG-conjugated Dynabeads (Invitrogen). Magnetic beads were washed five times with 1 ml of immunopurification buffer, and bound proteins were

eluted using 0.5 M NH$_4$OH and 0.5 mM EDTA. Elution was lyophilized in a speed-vac (Thermo Fisher Scientific), and the resulting pellet was resuspended in SDS-PAGE loading buffer. Purifications were optimized to use the mildest conditions that isolated only the wild-type Nup84 complex (Table S1) and none of the other nups with which it can coisolate (Alber et al., 2007a,b) so that we only probed interactions within the seven-protein complex. Several of the mild isolation conditions were explored for each purification to ensure that the maximum number of coisolating Nup84 components was detected. Isolated proteins were detected by R250 Coomassie staining and identified by matrix-assisted laser desorption/ionization (MALDI) MS analysis (Table S3; Alber et al., 2007a,b).

Truncated nups that were not able to interact with other Nup84 complex components were further analyzed by PAL to determine whether major misfolding was the main reason for the loss of interaction. PAL was performed as previously described (Dokudovskaya et al., 2006). In brief, immunopurified proteins (see above) still bound to the magnetic matrix were partially digested using Lys-C or Asp-N proteases. C-terminal fragments still bound to the matrix after digestion were eluted as described above and analyzed by Western blotting against the PrA moiety. The band pattern obtained was compared with the pattern generated by a wild-type nup treated in parallel.

Purification of native Nup84 complexes

To be able to purify the native Nup84 complex, we constructed strains in which the NUP-encoding gene was genomically tagged with PrA preceded by the human rhinovirus 3C protease (ppx) target sequence (GLEVLFQGPS). The sequence was introduced by PCR amplification of the transformation cassette from the plasmid pProtA/HIS5. We isolated the complex by affinity purification as previously described and released it from the affinity matrix by protease digestion. The recovered sample was then centrifuged at 20,000 g for 10 min. 50–100 µl of supernatant was loaded on top of a 5–20% sucrose gradient made in digestion buffer plus protease inhibitors. Gradients were ultracentrifuged on an SW 55 Ti rotor (Beckman Coulter) at 50,000 rpm and at 5°C for 7 h. Gradients were manually unloaded from the top in 12 fractions of 410 µl. Fractions were analyzed by SDS-PAGE, R250 Coomassie staining, and MS identification of the proteins. The six-member Nup84 complex (lacking Nup133; Siniossoglou et al., 2000) was isolated as previously described and purified by size-exclusion chromatography using a TSKgel G4000SW column (Tosoh Bioscience) in 20 mM Hepes/KOH, pH 7.4, 110 mM KOAc, 250 mM NaCl, 2 mM MgCl$_2$, 0.5% Triton X-100, and 0.1% Tween 20 buffer.

EM

Samples from selected fractions for EM were diluted to a concentration of ∼50 µg/ml. A 3-µl drop was applied to a carbon-coated grid that had not been previously glow discharged. The drop was blotted after ∼30 s and stained using three drops of 1% uranyl formate. The grid was air dried before observation in a transmission electron microscope (JEM-2100F; JEOL Ltd) operating at 200 kV. The images were collected using a low dose (∼6e/Å^2) on a 2k × 2k charge-coupled device camera (Tietz) with a defocus of 3 µm.

Images of individual particles were selected and classified using the program EMAN (Ludtke et al., 1999). 1,309 individual particles for the whole Nup84 complex, 799 for the Nup85(233–744) truncation complex, and 1,973 for the six-member complex (lacking Nup133) were selected for 2D image classification.

Representation of the Nup84 complex

Because few Nup84 complex components have full atomic resolution coverage, each nup was represented as a hybrid rigid body consisting of its crystallographic data (if available), comparative models (if an accurate alignment could be computed), or a string of beads mimicking the coarse shape of a related known fold. Regions not represented by either an atomic x-ray structure or a comparative model included linkers (up to 39 residues in length) and short segments at the termini (up to 62 residues in length); these regions were represented with a sphere for every 50 residues by approximating the average size of a 50-residue globular domain as previously described (Shen and Sali, 2006; Alber et al., 2007a). Where <50 residues needed to be represented, a smaller sphere size corresponding to that number of residues was used.

Conditional connectivity restraints from domain deletion data

We used affinity purification experiments with domain deletions to identify connected complexes (composites) containing a mix of whole proteins, protein fragments, and domains. In some cases, multiple such deletion composites overlap such that information contained by two or more composites

together cannot be derived by considering each composite separately. Here, we consider two such cases. First, if the same protein or set of proteins is lost in two different deletion experiments in which both of the deletions are performed on overlapping regions of a single protein, we deduce that the point of interaction for the lost protein or proteins is in the overlapping region. Second, if the same protein or set of proteins is lost in two different nonoverlapping truncations and a third composite contains all the lost proteins and both truncated regions, we deduce that the truncated regions must both interact with the lost proteins in the same location. Additional conditional connectivity restraints are added for these inferred interactions.

Restraint descriptions

S_{dm}. Each composite is encoded as a graph of nodes connected by edges. Each node represents a protein or a protein fragment, and each edge represents a possible interaction between connected nodes. Edges are generated for all possible interactions that might be implied by the corresponding pull-out experiment. An edge imposes a putative distance restraint, scoring well when the two potentially interacting proteins (or fragments) are actually interacting in the assessed assembly configuration and scoring poorly when the proteins (fragments) are too far apart to interact. For each composite graph, the best-scoring set of edges needed to connect the components of the pull-out composite is chosen by calculating a minimal spanning tree on the composite graph. Distance restraints for each of the minimal spanning tree edges are then added to the overall scoring function and thus used to drive the optimization of the complex. The connectivity of the complex selected by the connectivity restraint can change at each optimization step as the configuration of the complex changes.

S_{tri}. A structure is restrained to a bounding triangle as follows: (a) the two most distant points (points A and B) in the structure are chosen; (b) the most distant point (point C) to a line drawn between A and B (line L) measured along some line perpendicular to L (L_n) is chosen; and (c) the three distances between points A, B, and C are measured. The distances are ordered from largest to smallest and are restrained by a harmonic upper bound to match the corresponding distances in the target triangle.

S_{acc}. A Connolly surface is calculated for each component (Connolly, 1983). Interacting surfaces (those with at least two points within 5 Å) were scored using a two-part term that rewards the total number of surface atom pairs of within a distance cutoff and penalizes according to a weighted sum of all clashing pairs of atoms (Lasker et al., 2009).

S_{em}. The optimal projection of a model was found by enumerating all possible orientations (three angles) and positions (two translations) of the tested model relative to the class average and selecting the projection with the highest cross-correlation between the projected model density and the class average.

Sampling of good-scoring structures

Models that satisfied all restraints described in the previous section were obtained in four stages. Starting positions for the optimization were random configurations of the subunits and were chosen within a cube three times the length of the Nup84 complex along its principal component, as determined from the 2D EM class average. In the first coarse optimization stage, 100,000 coarse models were calculated by a Monte Carlo optimization of the sum of S_{dm} and S_{tri}, each starting from a different random initial configuration. In this stage, a Monte Carlo move consisted of either a two-degree rotation or 5-Å translation at a temperature of 273°C. Moves were accepted or rejected according to the Metropolis criterion: if S < 0, the move was always accepted; otherwise, the move was accepted with the probability of e$^{-S/T}$, in which S is the total score, and ΔS is the difference between the proposed total score and the previous score. Each optimization consisted of five Monte Carlo moves followed by 20 conjugate gradient refinement steps repeated 100 times for a total of 500 Monte Carlo moves and 2,000 conjugate gradient steps. In the second stage, the refinement stage, the models were refined by a Monte Carlo optimization of the sum of S_{acc}, S_{dm}, and S_{tri}, with smaller step sizes and with rotations limited to one degree and translations to 3.5 Å, with a total of 300 Monte Carlo steps. In the third stage, the filtering stage, the 10,000 top-scoring models were filtered by requiring sufficiently good alignment to the class averages of the EM images of the full and partial complex (Fig. 3, A and C). Finally, the remaining 9,479 structures were relaxed by optimizing the sum of S_{acc}, S_{dm}, S_{tri}, and S_{em} using the simplex algorithm (Nelder and Mead, 1965).

Ensemble analysis

Using the MODELLER-9v8 MALIGN3D command, the 9,479 good-scoring structures were aligned by minimizing the sum of squared distances between

equivalent pairs of C-α atoms to an iteratively updated average structure, pruning C-α distances between equivalent pairs longer than 10 Å (Sali and Blundell, 1993). The structures were then clustered by pair-wise C-α RMSD using single-linkage agglomerative hierarchical clustering showing a single dominant cluster of solutions. UCSF Chimera was used to visualize all molecular structures and density maps and to generate simulated density maps (Pettersen et al., 2004).

Building the Nup84 complex using only comparative models

Atomic structures of proteins are usually obtained through techniques such as x-ray crystallography and nuclear magnetic resonance spectroscopy. However, despite sterling efforts, experimentally determined atomic structures are still not available for the vast majority of the eukaryotic proteome. Fortunately, even when an experimentally determined structure is not available, a comparative model based on a related known structure can frequently be computed (Baker and Sali, 2001). In fact, with more than two orders of magnitude, more sequences can be modeled by comparative modeling than the number of experimentally determined structures (Pieper et al., 2011). Thus, a key question is how medium-resolution complex structures computed with crystallographic subunit structures, such as our Nup84 complex structure, differ from those computed with less accurate comparative models. We addressed this question for the Nup84 complex by computing the ensemble of the Nup84 complex structures using only comparative models of its subunits based on nonnup templates instead of crystallographic structures; flexible strings of beads were again used where model coverage was not available. All comparative models were generated with the program MODELLER-9v8 (Sali and Blundell, 1993) using target–template alignments from the fold assignment servers Phyre (Kelley and Sternberg, 2009) and pGenThreader (Ward et al., 2004). The ensemble of resulting Nup84 complex structures (Fig. S2 A) is clearly similar to that obtained with crystal structures (Fig. 5), thus demonstrating that our integrative approach can also be useful when only comparative models are used instead of experimentally determined atomic subunit structures.

Phenotypic analysis

To analyze the growth at different temperatures, strains were grown in liquid yeast extract peptone dextrose (YEPD) media overnight at 25°C, and cells were counted and diluted to a final concentration of 20,000 cells/ml. Four 10-fold serial dilutions were made and spotted on YEPD plates that were incubated at 25, 30, and 37°C for 1–2 d. Biological replicas of each experiment were performed. Plates were imaged using a LAS-3000 system (linear detection range; Fujifilm). Double-blinded semiquantitative estimation of growth was performed using MultiGauge (Fujifilm) and ImageJ (National Institutes of Health) software, which rendered similar results. In brief, the value (in arbitrary units) for each strain growth at each temperature was determined by adding the quantified density of the five 10-fold dilution spots. Values were normalized to each wild type, setting 100 arbitrary units as wild-type growth value (Tackett et al., 2005).

To analyze the Nup84 complex connectivity to the NPC core for each truncation mutant, affinity purifications were performed under buffer conditions that preserve those interactions in wild-type Nup84 complex PrA-tagged strains. Only mutants that showed NPC localization by immunofluorescence (Fig. S1) were used for the analysis. Affinity purifications were performed in parallel using the same buffer composition (20 mM Hepes, pH 7.4, 250 mM potassium acetate, 125 mM sodium chloride, 1% Triton X-100, 0.1% Tween 20, 2 mM magnesium chloride, and 1 mM DTT or 1.2 M ammonium acetate, pH 7.0, 0.5% Triton X-100, 0.1% Tween 20, and 1 mM DTT). Coomassie-stained SDS-PAGE–resolved bands were identified by MALDI MS. Nup159, Nup192, Nup188, Nup170, POM152, Nup157, Nup116, Nup100, Nsp1, and Nic96 were identified as the main bands. Bands corresponding to POM152, Nup116, Nup100, and Nsp1 were not quantified as a result of extensive overlapping. Band intensities were quantified in two independent experiments for each wild-type or mutant construct using the ImageJ gel tool. The amount of each protein, calibrated with a BSA standard, was transformed into molar amounts, and the relative molar ratio relative to the PrA-tagged handle for each mutant was normalized to the wild-type value and plotted into a bar graph. Divisions of 25% units were defined and assigned a color in the blue palette to generate a heat map for the NPC core connectivity within the Nup84 complex (see Fig. 7).

To analyze the NPC distribution, strains were transformed with plasmid pXYNUP49-CFP (Niepel et al., 2005). Strains expressing truncations Nup120(397–1037) and Nup133(531–1157), which showed synthetic sickness with plasmid pXYNUP49-CFP, were transformed with plasmid pBT029 (KAP121-CFP; Timney et al., 2006). Cells were grown in selective minimal media at 25°C to midlog phase and harvested by centrifugation.

Cells were visualized with a 63× 1.4 NA Plan-Apochromat objective using a microscope (Axioplan 2) equipped with a cooled charge-coupled device camera (ORCA-ER). The system was controlled with Openlab imaging software. Three image sections of several fields of cells in growth media were acquired at 0.5-μm increments. For semiquantitative quantification of the CFP signal distribution, n = 30 cells per strain were analyzed, double blinded, by selecting the image section that covered the higher area of nuclear signal for each cell. The NE contour was traced, and the cytoplasmic background-subtracted intensity of the CFP signal along the line contour was obtained using ImageJ. To determine the level of NPC clustering along the contour line, we calculated the coefficient of variation (CV; SD divided by the mean) of the signal intensity; the CV value decreases when the signal is evenly distributed along the NE and increases when the signal is clustered. Values were normalized to wild-type NPC distribution (CV = 0). To analyze the effect of increasing membrane fluidity over NPC clustering, strains were grown to early midlog phase and then transferred to fresh media or 0.4% BA containing fresh media (Scarcelli et al., 2007). Cells were grown for 1 h and then processed for fluorescence microscopy and NPC distribution as described above. Recovery after transfer to fresh media not including BA was tested after 4 h.

Online supplemental material

Fig. S1 shows the subcellular localization of the different Nup truncations determined by immunofluorescence. Fig. S2 shows an ensemble of structures for the Nup84 complex calculated using only homology models, a fitting of a single Nup84 complex structure into a published EM 3D map, an ensemble of structures for the Nup84 complex calculated using the published crystallographic interfaces as input restraints, and localization maps for Nup84 complex interaction interfaces compared with simulated electron density maps at a 1.5-nm resolution for the corresponding crystal structures. Fig. S3 shows the assignment of color codes and its mapping for both fitness and NPC clustering phenotypes. Fig. S4 shows that BA does not affect the overall stability of the Nup84 complex. Table S1 summarizes the Nup truncations used in this study and the conditions used for the affinity purification experiments shown in Fig. 1. Table S2 summarizes the strains used in this study. Table S3 shows the detailed MS analysis summarized in Fig. 1. Video 1 shows different views of the Nup84 complex ensemble and examples of single structures. Online supplemental material is available at http://www.jcb.org/cgi/content/full/jcb.201109008/DC1.

References

Aitchison, J.D., G. Blobel, and M.P. Rout. 1995. Nup120p: A yeast nucleoporin required for NPC distribution and mRNA transport. *J. Cell Biol.* 131:1659–1675. http://dx.doi.org/10.1083/jcb.131.6.1659

Alber, F., M.F. Kim, and A. Sali. 2005. Structural characterization of assemblies from overall shape and subcomplex compositions. *Structure.* 13:435–445. http://dx.doi.org/10.1016/j.str.2005.01.013

Alber, F., S. Dokudovskaya, L.M. Veenhoff, W. Zhang, J. Kipper, D. Devos, A. Suprapto, O. Karni-Schmidt, R. Williams, B.T. Chait, et al. 2007a. Determining the architectures of macromolecular assemblies. *Nature.* 450:683–694. http://dx.doi.org/10.1038/nature06404

Alber, F., S. Dokudovskaya, L.M. Veenhoff, W. Zhang, J. Kipper, D. Devos, A. Suprapto, O. Karni-Schmidt, R. Williams, B.T. Chait, et al. 2007b. The molecular architecture of the nuclear pore complex. *Nature.* 450:695–701. http://dx.doi.org/10.1038/nature06405

Alber, F., F. Förster, D. Korkin, M. Topf, and A. Sali. 2008. Integrating diverse data for structure determination of macromolecular assemblies. *Annu. Rev. Biochem.* 77:443–477. http://dx.doi.org/10.1146/annurev.biochem.77.060407.135530

Amlacher, S., P. Sarges, D. Flemming, V. van Noort, R. Kunze, D.P. Devos, M. Arumugam, P. Bork, and E. Hurt. 2011. Insight into structure and assembly

of the nuclear pore complex by utilizing the genome of a eukaryotic thermophile. *Cell*. 146:277–289. http://dx.doi.org/10.1016/j.cell.2011.06.039

Baker, D., and A. Sali. 2001. Protein structure prediction and structural genomics. *Science*. 294:93–96. http://dx.doi.org/10.1126/science.1065659

Beck, M., F. Förster, M. Ecke, J.M. Plitzko, F. Melchior, G. Gerisch, W. Baumeister, and O. Medalia. 2004. Nuclear pore complex structure and dynamics revealed by cryoelectron tomography. *Science*. 306:1387–1390. http://dx.doi.org/10.1126/science.1104808

Belgareh, N., and V. Doye. 1997. Dynamics of nuclear pore distribution in nucleoporin mutant yeast cells. *J. Cell Biol.* 136:747–759. http://dx.doi.org/10.1083/jcb.136.4.747

Belgareh, N., G. Rabut, S.W. Baï, M. van Overbeek, J. Beaudouin, N. Daigle, O.V. Zatsepina, F. Pasteau, V. Labas, M. Fromont-Racine, et al. 2001. An evolutionarily conserved NPC subcomplex, which redistributes in part to kinetochores in mammalian cells. *J. Cell Biol.* 154:1147–1160. http://dx.doi.org/10.1083/jcb.200101081

Boehmer, T., J. Enninga, S. Dales, G. Blobel, and H. Zhong. 2003. Depletion of a single nucleoporin, Nup107, prevents the assembly of a subset of nucleoporins into the nuclear pore complex. *Proc. Natl. Acad. Sci. USA*. 100:981–985. http://dx.doi.org/10.1073/pnas.252749899

Boehmer, T., S. Jeudy, I.C. Berke, and T.U. Schwartz. 2008. Structural and functional studies of Nup107/Nup133 interaction and its implications for the architecture of the nuclear pore complex. *Mol. Cell*. 30:721–731. http://dx.doi.org/10.1016/j.molcel.2008.04.022

Brohawn, S.G., and T.U. Schwartz. 2009. Molecular architecture of the Nup84-Nup145C-Sec13 edge element in the nuclear pore complex lattice. *Nat. Struct. Mol. Biol.* 16:1173–1177. http://dx.doi.org/10.1038/nsmb.1713

Brohawn, S.G., N.C. Leksa, E.D. Spear, K.R. Rajashankar, and T.U. Schwartz. 2008. Structural evidence for common ancestry of the nuclear pore complex and vesicle coats. *Science*. 322:1369–1373. http://dx.doi.org/10.1126/science.1165886

Brohawn, S.G., J.R. Partridge, J.R. Whittle, and T.U. Schwartz. 2009. The nuclear pore complex has entered the atomic age. *Structure*. 17:1156–1168. http://dx.doi.org/10.1016/j.str.2009.07.014

Bucci, M., and S.R. Wente. 1997. In vivo dynamics of nuclear pore complexes in yeast. *J. Cell Biol.* 136:1185–1199. http://dx.doi.org/10.1083/jcb.136.6.1185

Chen, Z.A., A. Jawhari, L. Fischer, C. Buchen, S. Tahir, T. Kamenski, M. Rasmussen, L. Lariviere, J.C. Bukowski-Wills, M. Nilges, et al. 2010. Architecture of the RNA polymerase II-TFIIF complex revealed by cross-linking and mass spectrometry. *EMBO J.* 29:717–726. http://dx.doi.org/10.1038/emboj.2009.401

Connolly, M.L. 1983. Solvent-accessible surfaces of proteins and nucleic acids. *Science*. 221:709–713. http://dx.doi.org/10.1126/science.6879170

D'Angelo, M.A., and M.W. Hetzer. 2008. Structure, dynamics and function of nuclear pore complexes. *Trends Cell Biol.* 18:456–466. http://dx.doi.org/10.1016/j.tcb.2008.07.009

Das, R., and D. Baker. 2008. Macromolecular modeling with rosetta. *Annu. Rev. Biochem.* 77:363–382. http://dx.doi.org/10.1146/annurev.biochem.77.062906.171838

Debler, E.W., Y. Ma, H.S. Seo, K.C. Hsia, T.R. Noriega, G. Blobel, and A. Hoelz. 2008. A fence-like coat for the nuclear pore membrane. *Mol. Cell*. 32:815–826. http://dx.doi.org/10.1016/j.molcel.2008.12.001

DeGrasse, J.A., K.N. DuBois, D. Devos, T.N. Siegel, A. Sali, M.C. Field, M.P. Rout, and B.T. Chait. 2009. Evidence for a shared nuclear pore complex architecture that is conserved from the last common eukaryotic ancestor. *Mol. Cell. Proteomics*. 8:2119–2130. http://dx.doi.org/10.1074/mcp.M900038-MCP200

Devos, D., S. Dokudovskaya, F. Alber, R. Williams, B.T. Chait, A. Sali, and M.P. Rout. 2004. Components of coated vesicles and nuclear pore complexes share a common molecular architecture. *PLoS Biol.* 2:e380. http://dx.doi.org/10.1371/journal.pbio.0020380

Devos, D., S. Dokudovskaya, R. Williams, F. Alber, N. Eswar, B.T. Chait, M.P. Rout, and A. Sali. 2006. Simple fold composition and modular architecture of the nuclear pore complex. *Proc. Natl. Acad. Sci. USA*. 103:2172–2177. http://dx.doi.org/10.1073/pnas.0506345103

Dokudovskaya, S., R. Williams, D. Devos, A. Sali, B.T. Chait, and M.P. Rout. 2006. Protease accessibility laddering: A proteomic tool for probing protein structure. *Structure*. 14:653–660. http://dx.doi.org/10.1016/j.str.2006.02.006

Dokudovskaya, S., F. Waharte, A. Schlessinger, U. Pieper, D.P. Devos, I.M. Cristea, R. Williams, J. Salamero, B.T. Chait, A. Sali, et al. 2011. A conserved coatomer-related complex containing Sec13 and Seh1 dynamically associates with the vacuole in *Saccharomyces cerevisiae*. *Mol. Cell. Proteomics*. 10:M110: 006478. http://dx.doi.org/10.1074/mcp.M110.006478

Doye, V., and E.C. Hurt. 1995. Genetic approaches to nuclear pore structure and function. *Trends Genet.* 11:235–241. http://dx.doi.org/10.1016/S0168-9525(00)89057-5

Doye, V., R. Wepf, and E.C. Hurt. 1994. A novel nuclear pore protein Nup133p with distinct roles in poly(A)+ RNA transport and nuclear pore distribution. *EMBO J.* 13:6062–6075.

Dultz, E., E. Zanin, C. Wurzenberger, M. Braun, G. Rabut, L. Sironi, and J. Ellenberg. 2008. Systematic kinetic analysis of mitotic dis- and reassembly of the nuclear pore in living cells. *J. Cell Biol.* 180:857–865. http://dx.doi.org/10.1083/jcb.200707026

Fabre, E., and E. Hurt. 1997. Yeast genetics to dissect the nuclear pore complex and nucleocytoplasmic trafficking. *Annu. Rev. Genet.* 31:277–313. http://dx.doi.org/10.1146/annurev.genet.31.1.277

Fath, S., J.D. Mancias, X. Bi, and J. Goldberg. 2007. Structure and organization of coat proteins in the COPII cage. *Cell*. 129:1325–1336. http://dx.doi.org/10.1016/j.cell.2007.05.036

Field, M.C., A. Sali, and M.P. Rout. 2011. Evolution: On a bender—BARs, ESCRTs, COPs, and finally getting your coat. *J. Cell Biol.* 193:963–972. http://dx.doi.org/10.1083/jcb.201102042

Fotin, A., Y. Cheng, P. Sliz, N. Grigorieff, S.C. Harrison, T. Kirchhausen, and T. Walz. 2004. Molecular model for a complete clathrin lattice from electron cryomicroscopy. *Nature*. 432:573–579. http://dx.doi.org/10.1038/nature03079

Gordon, L.M., R.D. Sauerheber, J.A. Esgate, I. Dipple, R.J. Marchmont, and M.D. Houslay. 1980. The increase in bilayer fluidity of rat liver plasma membranes achieved by the local anesthetic benzyl alcohol affects the activity of intrinsic membrane enzymes. *J. Biol. Chem.* 255:4519–4527.

Gueldener, U., J. Heinisch, G.J. Koehler, D. Voss, and J.H. Hegemann. 2002. A second set of loxP marker cassettes for Cre-mediated multiple gene knockouts in budding yeast. *Nucleic Acids Res.* 30:e23. http://dx.doi.org/10.1093/nar/30.6.e23

Heath, C.V., C.S. Copeland, D.C. Amberg, V. Del Priore, M. Snyder, and C.N. Cole. 1995. Nuclear pore complex clustering and nuclear accumulation of poly(A)+ RNA associated with mutation of the *Saccharomyces cerevisiae* RAT2/NUP120 gene. *J. Cell Biol.* 131:1677–1697. http://dx.doi.org/10.1083/jcb.131.6.1677

Hsia, K.C., P. Stavropoulos, G. Blobel, and A. Hoelz. 2007. Architecture of a coat for the nuclear pore membrane. *Cell*. 131:1313–1326. http://dx.doi.org/10.1016/j.cell.2007.11.038

Kampmann, M., and G. Blobel. 2009. Three-dimensional structure and flexibility of a membrane-coating module of the nuclear pore complex. *Nat. Struct. Mol. Biol.* 16:782–788. http://dx.doi.org/10.1038/nsmb.1618

Kampmann, M., C.E. Atkinson, A.L. Mattheyses, and S.M. Simon. 2011. Mapping the orientation of nuclear pore proteins in living cells with polarized fluorescence microscopy. *Nat. Struct. Mol. Biol.* 18:643–649. http://dx.doi.org/10.1038/nsmb.2056

Kelley, L.A., and M.J. Sternberg. 2009. Protein structure prediction on the Web: A case study using the Phyre server. *Nat. Protoc.* 4:363–371. http://dx.doi.org/10.1038/nprot.2009.2

Krull, S., J. Thyberg, B. Björkroth, H.R. Rackwitz, and V.C. Cordes. 2004. Nucleoporins as components of the nuclear pore complex core structure and Tpr as the architectural element of the nuclear basket. *Mol. Biol. Cell*. 15:4261–4277. http://dx.doi.org/10.1091/mbc.E04-03-0165

Lasker, K., M. Topf, A. Sali, and H.J. Wolfson. 2009. Inferential optimization for simultaneous fitting of multiple components into a CryoEM map of their assembly. *J. Mol. Biol.* 388:180–194. http://dx.doi.org/10.1016/j.jmb.2009.02.031

Lasker, K., J.L. Phillips, D. Russel, J. Velázquez-Muriel, D. Schneidman-Duhovny, E. Tjioe, B. Webb, A. Schlessinger, and A. Sali. 2010. Integrative structure modeling of macromolecular assemblies from proteomics data. *Mol. Cell. Proteomics*. 9:1689–1702. http://dx.doi.org/10.1074/mcp.R110.000067

Lee, C., and J. Goldberg. 2010. Structure of coatomer cage proteins and the relationship among COPI, COPII, and clathrin vesicle coats. *Cell*. 142:123–132. http://dx.doi.org/10.1016/j.cell.2010.05.030

Leksa, N.C., S.G. Brohawn, and T.U. Schwartz. 2009. The structure of the scaffold nucleoporin Nup120 reveals a new and unexpected domain architecture. *Structure*. 17:1082–1091. http://dx.doi.org/10.1016/j.str.2009.06.003

Li, O., C.V. Heath, D.C. Amberg, T.C. Dockendorff, C.S. Copeland, M. Snyder, and C.N. Cole. 1995. Mutation or deletion of the *Saccharomyces cerevisiae* RAT3/NUP133 gene causes temperature-dependent nuclear accumulation of poly(A)+ RNA and constitutive clustering of nuclear pore complexes. *Mol. Biol. Cell*. 6:401–417.

Liu, H.L., C.P. De Souza, A.H. Osmani, and S.A. Osmani. 2009. The three fungal transmembrane nuclear pore complex proteins of *Aspergillus nidulans* are dispensable in the presence of an intact An-Nup84-120 complex. *Mol. Biol. Cell*. 20:616–630. http://dx.doi.org/10.1091/mbc.E08-06-0628

Loïodice, I., A. Alves, G. Rabut, M. Van Overbeek, J. Ellenberg, J.B. Sibarita, and V. Doye. 2004. The entire Nup107-160 complex, including three new members, is targeted as one entity to kinetochores in mitosis. *Mol. Biol. Cell.* 15:3333–3344. http://dx.doi.org/10.1091/mbc.E03-12-0878

Longtine, M.S., A. McKenzie III, D.J. Demarini, N.G. Shah, A. Wach, A. Brachat, P. Philippsen, and J.R. Pringle. 1998. Additional modules for versatile and economical PCR-based gene deletion and modification in *Saccharomyces cerevisiae. Yeast.* 14:953–961. http://dx.doi.org/10.1002/(SICI)1097-0061(199807)14:10<953::AID-YEA293>3.0.CO;2-U

Ludtke, S.J., P.R. Baldwin, and W. Chiu. 1999. EMAN: Semiautomated software for high-resolution single-particle reconstructions. *J. Struct. Biol.* 128:82–97. http://dx.doi.org/10.1006/jsbi.1999.4174

Lutzmann, M., R. Kunze, A. Buerer, U. Aebi, and E. Hurt. 2002. Modular self-assembly of a Y-shaped multiprotein complex from seven nucleoporins. *EMBO J.* 21:387–397. http://dx.doi.org/10.1093/emboj/21.3.387

Lutzmann, M., R. Kunze, K. Stangl, P. Stelter, K.F. Tóth, B. Böttcher, and E. Hurt. 2005. Reconstitution of Nup157 and Nup145N into the Nup84 complex. *J. Biol. Chem.* 280:18442–18451. http://dx.doi.org/10.1074/jbc.M412787200

McMahon, H.T., and I.G. Mills. 2004. COP and clathrin-coated vesicle budding: Different pathways, common approaches. *Curr. Opin. Cell Biol.* 16:379–391. http://dx.doi.org/10.1016/j.ceb.2004.06.009

Miele, A.E., P.J. Watson, P.R. Evans, L.M. Traub, and D.J. Owen. 2004. Two distinct interaction motifs in amphiphysin bind two independent sites on the clathrin terminal domain beta-propeller. *Nat. Struct. Mol. Biol.* 11:242–248. http://dx.doi.org/10.1038/nsmb736

Nagy, V., K.C. Hsia, E.W. Debler, M. Kampmann, A.M. Davenport, G. Blobel, and A. Hoelz. 2009. Structure of a trimeric nucleoporin complex reveals alternate oligomerization states. *Proc. Natl. Acad. Sci. USA.* 106:17693–17698. http://dx.doi.org/10.1073/pnas.0909373106

Nelder, J.A., and R. Mead. 1965. A simplex method for function minimization. *The Computer Journal.* 7:308–313.

Niepel, M., C. Strambio-de-Castillia, J. Fasolo, B.T. Chait, and M.P. Rout. 2005. The nuclear pore complex–associated protein, Mlp2p, binds to the yeast spindle pole body and promotes its efficient assembly. *J. Cell Biol.* 170:225–235. http://dx.doi.org/10.1083/jcb.200504140

Oeffinger, M., K.E. Wei, R. Rogers, J.A. DeGrasse, B.T. Chait, J.D. Aitchison, and M.P. Rout. 2007. Comprehensive analysis of diverse ribonucleoprotein complexes. *Nat. Methods.* 4:951–956. http://dx.doi.org/10.1038/nmeth1101

Pemberton, L.F., M.P. Rout, and G. Blobel. 1995. Disruption of the nucleoporin gene NUP133 results in clustering of nuclear pore complexes. *Proc. Natl. Acad. Sci. USA.* 92:1187–1191. http://dx.doi.org/10.1073/pnas.92.4.1187

Peters, R. 2009. Translocation through the nuclear pore: Kaps pave the way. *Bioessays.* 31:466–477. http://dx.doi.org/10.1002/bies.200800159

Pettersen, E.F., T.D. Goddard, C.C. Huang, G.S. Couch, D.M. Greenblatt, E.C. Meng, and T.E. Ferrin. 2004. UCSF Chimera—a visualization system for exploratory research and analysis. *J. Comput. Chem.* 25:1605–1612. http://dx.doi.org/10.1002/jcc.20084

Pieper, U., B.M. Webb, D.T. Barkan, D. Schneidman-Duhovny, A. Schlessinger, H. Braberg, Z. Yang, E.C. Meng, E.F. Pettersen, C.C. Huang, et al. 2011. ModBase, a database of annotated comparative protein structure models, and associated resources. *Nucleic Acids Res.* 39(Database issue):D465–D474. http://dx.doi.org/10.1093/nar/gkq1091

Robinson, C.V., A. Sali, and W. Baumeister. 2007. The molecular sociology of the cell. *Nature.* 450:973–982. http://dx.doi.org/10.1038/nature06523

Rout, M.P., J.D. Aitchison, A. Suprapto, K. Hjertaas, Y. Zhao, and B.T. Chait. 2000. The yeast nuclear pore complex: Composition, architecture, and transport mechanism. *J. Cell Biol.* 148:635–651. http://dx.doi.org/10.1083/jcb.148.4.635

Salama, N.R., J.S. Chuang, and R.W. Schekman. 1997. Sec31 encodes an essential component of the COPII coat required for transport vesicle budding from the endoplasmic reticulum. *Mol. Biol. Cell.* 8:205–217.

Sali, A., and T.L. Blundell. 1993. Comparative protein modelling by satisfaction of spatial restraints. *J. Mol. Biol.* 234:779–815. http://dx.doi.org/10.1006/jmbi.1993.1626

Sampathkumar, P., T. Gheyi, S.A. Miller, K.T. Bain, M. Dickey, J.B. Bonanno, S.J. Kim, J. Phillips, U. Pieper, J. Fernandez-Martinez, et al. 2011. Structure of the C-terminal domain of *Saccharomyces cerevisiae* Nup133, a component of the nuclear pore complex. *Proteins.* 79:1672–1677. http://dx.doi.org/10.1002/prot.22973

Scarcelli, J.J., C.A. Hodge, and C.N. Cole. 2007. The yeast integral membrane protein Apq12 potentially links membrane dynamics to assembly of nuclear pore complexes. *J. Cell Biol.* 178:799–812. http://dx.doi.org/10.1083/jcb.200702120

Seo, H.S., Y. Ma, E.W. Debler, D. Wacker, S. Kutik, G. Blobel, and A. Hoelz. 2009. Structural and functional analysis of Nup120 suggests ring formation of the Nup84 complex. *Proc. Natl. Acad. Sci. USA.* 106:14281–14286. http://dx.doi.org/10.1073/pnas.0907453106

Shen, M.Y., and A. Sali. 2006. Statistical potential for assessment and prediction of protein structures. *Protein Sci.* 15:2507–2524. http://dx.doi.org/10.1110/ps.062416606

Siniossoglou, S., C. Wimmer, M. Rieger, V. Doye, H. Tekotte, C. Weise, S. Emig, A. Segref, and E.C. Hurt. 1996. A novel complex of nucleoporins, which includes Sec13p and a Sec13p homolog, is essential for normal nuclear pores. *Cell.* 84:265–275. http://dx.doi.org/10.1016/S0092-8674(00)80981-2

Siniossoglou, S., M. Lutzmann, H. Santos-Rosa, K. Leonard, S. Mueller, U. Aebi, and E. Hurt. 2000. Structure and assembly of the Nup84p complex. *J. Cell Biol.* 149:41–54. http://dx.doi.org/10.1083/jcb.149.1.41

Stagg, S.M., P. LaPointe, A. Razvi, C. Gürkan, C.S. Potter, B. Carragher, and W.E. Balch. 2008. Structural basis for cargo regulation of COPII coat assembly. *Cell.* 134:474–484. http://dx.doi.org/10.1016/j.cell.2008.06.024

Stoffler, D., B. Feja, B. Fahrenkrog, J. Walz, D. Typke, and U. Aebi. 2003. Cryo-electron tomography provides novel insights into nuclear pore architecture: Implications for nucleocytoplasmic transport. *J. Mol. Biol.* 328:119–130. http://dx.doi.org/10.1016/S0022-2836(03)00266-3

Strambio-De-Castillia, C., M. Niepel, and M.P. Rout. 2010. The nuclear pore complex: Bridging nuclear transport and gene regulation. *Nat. Rev. Mol. Cell Biol.* 11:490–501. http://dx.doi.org/10.1038/nrm2928

Strawn, L.A., T. Shen, N. Shulga, D.S. Goldfarb, and S.R. Wente. 2004. Minimal nuclear pore complexes define FG repeat domains essential for transport. *Nat. Cell Biol.* 6:197–206. http://dx.doi.org/10.1038/ncb1097

Tackett, A.J., D.J. Dilworth, M.J. Davey, M. O'Donnell, J.D. Aitchison, M.P. Rout, and B.T. Chait. 2005. Proteomic and genomic characterization of chromatin complexes at a boundary. *J. Cell Biol.* 169:35–47. http://dx.doi.org/10.1083/jcb.200502104

Teixeira, M.T., E. Fabre, and B. Dujon. 1999. Self-catalyzed cleavage of the yeast nucleoporin Nup145p precursor. *J. Biol. Chem.* 274:32439–32444. http://dx.doi.org/10.1074/jbc.274.45.32439

ter Haar, E., S.C. Harrison, and T. Kirchhausen. 2000. Peptide-in-groove interactions link target proteins to the beta-propeller of clathrin. *Proc. Natl. Acad. Sci. USA.* 97:1096–1100. http://dx.doi.org/10.1073/pnas.97.3.1096

Timney, B.L., J. Tetenbaum-Novatt, D.S. Agate, R. Williams, W. Zhang, B.T. Chait, and M.P. Rout. 2006. Simple kinetic relationships and nonspecific competition govern nuclear import rates in vivo. *J. Cell Biol.* 175:579–593. http://dx.doi.org/10.1083/jcb.200608141

Titus, L.C., T.R. Dawson, D.J. Rexer, K.J. Ryan, and S.R. Wente. 2010. Members of the RSC chromatin-remodeling complex are required for maintaining proper nuclear envelope structure and pore complex localization. *Mol. Biol. Cell.* 21:1072–1087. http://dx.doi.org/10.1091/mbc.E09-07-0615

Vasu, S., S. Shah, A. Orjalo, M. Park, W.H. Fischer, and D.J. Forbes. 2001. Novel vertebrate nucleoporins Nup133 and Nup160 play a role in mRNA export. *J. Cell Biol.* 155:339–354. http://dx.doi.org/10.1083/jcb.200108007

Ward, J.J., L.J. McGuffin, K. Bryson, B.F. Buxton, and D.T. Jones. 2004. The DISOPRED server for the prediction of protein disorder. *Bioinformatics.* 20:2138–2139. http://dx.doi.org/10.1093/bioinformatics/bth195

Wente, S.R., M.P. Rout, and G. Blobel. 1992. A new family of yeast nuclear pore complex proteins. *J. Cell Biol.* 119:705–723. http://dx.doi.org/10.1083/jcb.119.4.705

Whittle, J.R., and T.U. Schwartz. 2009. Architectural nucleoporins Nup157/170 and Nup133 are structurally related and descend from a second ancestral element. *J. Biol. Chem.* 284:28442–28452. http://dx.doi.org/10.1074/jbc.M109.023580

Yang, Q., M.P. Rout, and C.W. Akey. 1998. Three-dimensional architecture of the isolated yeast nuclear pore complex: Functional and evolutionary implications. *Mol. Cell.* 1:223–234. http://dx.doi.org/10.1016/S1097-2765(00)80023-4

Zhou, M., A.M. Sandercock, C.S. Fraser, G. Ridlova, E. Stephens, M.R. Schenauer, T. Yokoi-Fong, D. Barsky, J.A. Leary, J.W. Hershey, et al. 2008. Mass spectrometry reveals modularity and a complete subunit interaction map of the eukaryotic translation factor eIF3. *Proc. Natl. Acad. Sci. USA.* 105:18139–18144. http://dx.doi.org/10.1073/pnas.0801313105